

AD A 1.38066



PASSIVE INFRARED RANGING

THESIS

Norman K. Leonpacher  
Captain, USAF

AFIT/GEP/PH/83D-5

This document has been approved  
for public release and sale; its  
distribution is unlimited.

DEPARTMENT OF THE AIR FORCE  
AIR UNIVERSITY

**AIR FORCE INSTITUTE OF TECHNOLOGY**

Wright-Patterson Air Force Base, Ohio

DTIC

LECTE

FEB 22 1984

A

DTIC FILE COPY

84 02 21 175

AFIT/GEP/PH/83D-5

PASSIVE INFRARED RANGING

THESIS

Norman K. Leonpacher  
Captain, USAF

AFIT/GEP/PH/83D-5

This document has been approved  
for public release and sale; its  
distribution is unlimited

DTIC  
ELECTE

FEB 22 1984

A

PASSIVE INFRARED RANGING

THESIS

Presented to the Faculty of the School of Engineering  
of the Air Force Institute of Technology

Air University

In Partial Fulfillment of the  
Requirements for the Degree of  
Master of Science in Engineering Physics



Norman K. Leonpacher, B.S.  
Captain, USAF

December 1983

Accession For	
NTIS GRA&I	<input checked="" type="checkbox"/>
DTIC TAB	<input type="checkbox"/>
Unannounced	<input type="checkbox"/>
Justification	
Distribution/	
Availability Codes	
Avail and/or	
Special	

AI

Approved for public release; distribution unlimited

## Preface

The purpose of this study was to show that the range of an infrared source can be estimated by analyzing its spectral signature. Although a limited number of source spectra were available to develop and test the ranging algorithm, a method has been established that can be expanded upon if more data becomes available.

The VAX computer system at Air Force Wright Aeronautical Laboratories (AFWAL), Wright-Patterson AFB, Ohio, was used extensively in developing the algorithm. Spectral data files, and computer programs to read these files, were available before this study began. Many new programs that have been written are extensions of these existing programs. Others are straightforward applications of the ideas in the text, and none are significant enough to be included in the report. File copies, however, are available through Dr. R. B. Sanderson, AFWAL/AAWP-1, Wright-Patterson AFB, Ohio.

Studies of this magnitude would not be possible in the limited time available without the assistance of others. I would like to thank Dr. R. B. Sanderson of the Air Force Wright Aeronautics Lab for his guidance and insight that were instrumental to the success of this project. I would also like to thank Nick Pequiot for his assistance with the AFWAL computer. A word of thanks is also owed to my faculty advisor, Maj Dave Graham, for his help throughout the

project. And finally, I would like to express deep gratitude to my wife Carolyn for her patience and inspiration that are indeed an integral part of this thesis.

Norman K. Leonpacher

## Table of Contents

	Page
Preface . . . . .	ii
List of Figures . . . . .	vi
List of Tables . . . . .	viii
Abstract . . . . .	ix
I. Introduction . . . . .	1
Background . . . . .	1
Problem . . . . .	1
Approach . . . . .	2
Assumptions and Limitations . . . . .	4
II. Infrared Signatures . . . . .	6
Source Types . . . . .	6
Atmospherics . . . . .	12
Background Contributions . . . . .	13
Computer Files . . . . .	14
III. Spectral Discrimination . . . . .	22
Pattern Recognition . . . . .	22
Gaussian Statistics . . . . .	25
Cluster Discrimination . . . . .	27
Intensity Normalization . . . . .	29
IV. Spectral Optimization . . . . .	31
Band Selection . . . . .	31
Bhattacharyya Measure . . . . .	33
Background Fluctuations . . . . .	41
V. Ranging Algorithm . . . . .	47
Development . . . . .	47
Testing . . . . .	53
VI. Conclusion . . . . .	59
Summary . . . . .	59
Recommendations . . . . .	61
Appendix A: Linear Decision Functions . . . . .	63
Appendix B: Computed Data for ARI Files . . . . .	66

Appendix C: Noise Variance . . . . .	71
Appendix D: Transforms of Band Variation to Angular Variation . . . . .	76
Bibliography . . . . .	78
Vita . . . . .	80

## List of Figures

Figure	Page
1. Intensity of 1000 K Blackbody at 0, 1, and 10 km . .	3
2. Intensity of Blackbodies at Several Temperatures . .	8
3. Typical Missile Spectrum (ARI #003) . . . . .	10
4. Aircraft Spectrum at Different Power Settings . . .	11
5a. ARI Missile Spectrum (ARI #003) . . . . .	15
5b. ARI Flare Spectrum (#017) . . . . .	16
5c. ARI Flare Spectrum (#050) . . . . .	16
6a. AFG Coke Oven Spectrum (#003) . . . . .	19
6b. AFG Hot Metal Spectrum (#009) . . . . .	19
6c. AFG Smoke Stack Spectrum (#010) . . . . .	20
6d. AFG Hot Building Spectrum (#014) . . . . .	20
7. Spectral Classes in Color Space . . . . .	23
8. Decision Boundaries for Normal Distributions . . . .	24
9. LOWTRAN Model Comparison at 2 km . . . . .	32
10. LOWTRAN Range Comparison for Model 6 . . . . .	33
11. Bhattacharyya Separation for Blackbody Sources Using Two Colors . . . . .	36
12. Bhattacharyya Separation for ARI Sources Using Two Colors . . . . .	38
13. Range Distributions for ARI Sources Using Three Colors . . . . .	40
14. Bhattacharyya Separation for ARI Sources Using Three Colors . . . . .	40
15. Bhattacharyya Separation for ARI Sources with Noise Added . . . . .	44
16. Range Resolution of ARI Sources with Noise Added . .	46



17.	Mean of Each Range Distribution . . . . .	48
18.	Range of Each Distribution . . . . .	49
19.	Slope of Decision Boundary Between Distributions . .	50
20.	Projection of Unknown Sources Along Decision Boundaries . . . . .	51
21.	Location of AFG Files in Color Space . . . . .	55
22.	Typical Window Function . . . . .	73

List of Tables

Table	Page
I. Aerodyne Research Inc. Files . . . . .	15
II. Air Force Geophysics Lab Files . . . . .	18
III. Computed Ranges for ARI Files . . . . .	54
IV. Range Comparison for AFG Files . . . . .	56
V. ARI Computed Data . . . . .	68

Abstract

↙  $1/\text{cm}$   
The range of an infrared source was estimated by analyzing the atmospheric absorption by  $\text{CO}_2$  in several wavelength intervals of its spectrum. These bandpasses were located at the edge of the  $\text{CO}_2$  absorption band near  $2300 \text{ cm}^{-1}$  (4.3 <sup>micron</sup> ~~μm~~).

A specific algorithm to predict range was determined based on numerous computer generated spectra. When tested with these spectra, range estimates within 0.8 km were obtained for ranges between 0 and 18 km.

Accuracy decreased when actual source spectra were tested. Although actual spectra were available only for ranges to 5 km, 63% of these spectra resulted in range estimates that were within 1.6 km of the actual range. Specific spectral conditions that affected the range predictions were found. Methods to correct the deficiencies were discussed.

Errors from atmospheric variations, and the effects of background noise, were also investigated. Limits on accuracy and range resolution were determined.

## I. Introduction

### Background

Any aircraft that flies into a combat environment is likely to become a target for enemy weapons. Because of its lethal warhead and precision guidance, the surface-to-air missile is probably the most deadly weapon. When the rocket motor of the missile burns, it emits intense radiation in the infrared region of the electromagnetic spectrum. Infrared receivers are being developed to provide reliable warning of a missile launch.

In addition to providing a launch warning, it may be possible for detectors to give an indication of how far away an infrared source is. Radiation is attenuated as it travels through the atmosphere, and its spectral profile is altered. The constituents of the atmosphere absorb at different frequencies, and the amount of absorption depends on transmission range and the concentration of each particle. If a particular atmospheric model is assumed, the spectral signature of a detected infrared signal can be compared with a known spectral signature to give an indication of transmission range.

### Problem

Specific frequency bands to use for comparison of infrared signatures are sought. When two or more bands are

compared, statistical distributions are formed that represent spectra of sources of the same range. The separation between these distributions is optimized by adjusting the frequency and bandwidth of each spectral band. A ranging algorithm that predicts the range of an unknown source is determined based on existing target spectra and an atmospheric transmission model called LOWTRAN (Ref 1).

### Approach

In order to develop the computer programs required to analyze spectral signatures, targets are initially assumed to be blackbody radiators. The radiant exitance for blackbodies is easily calculated from Planck's law (Ref 2:126), and is spectrally multiplied by LOWTRAN transmittance to simulate range. The resulting spectra allow development of the analysis under controlled input conditions.

An example of the radiance of a 1000 K blackbody between 2000 and 2500  $\text{cm}^{-1}$  (4-5  $\mu\text{m}$ ) multiplied by two different LOWTRAN ranges is shown in Figure 1. The attenuation of the signal between 2200 and 2300  $\text{cm}^{-1}$  is from  $\text{CO}_2$  in the atmosphere. The total amount of attenuation is related to the range of the source, but so is the relative attenuation between frequencies. An indication of range can be obtained by comparing the relative signal intensity between 2100 and 2200  $\text{cm}^{-1}$  to the intensity between 2200 and 2300  $\text{cm}^{-1}$ . If the intensities are nearly equal, the

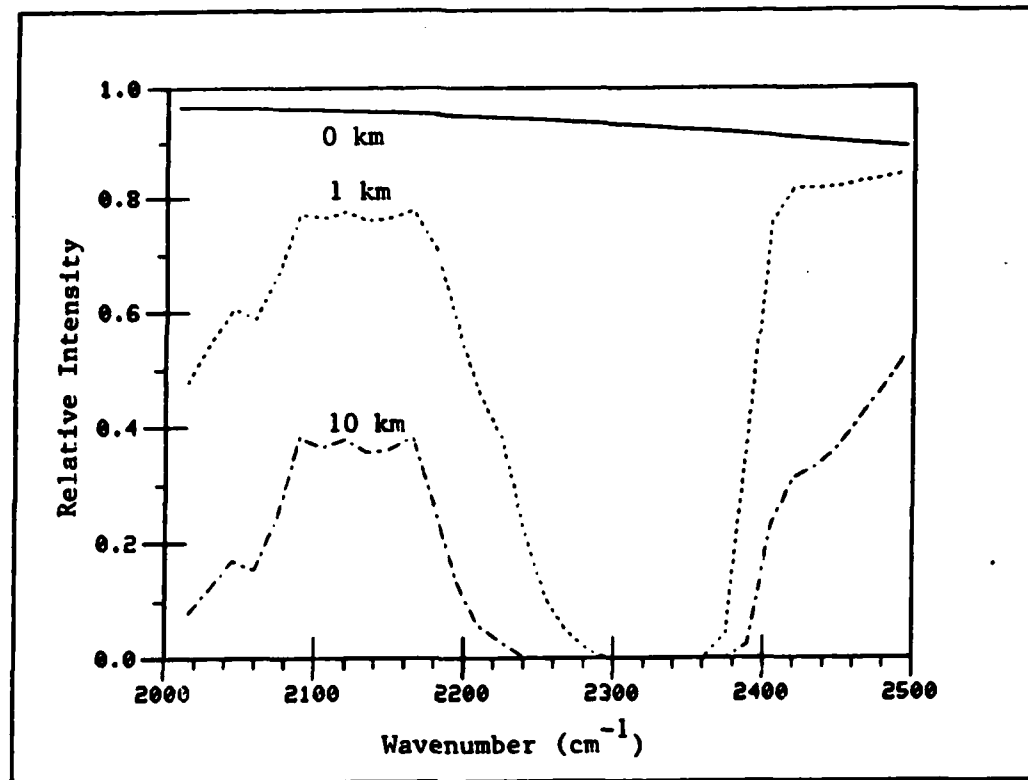


Figure 1. Intensity of 1000 K Blackbody at 0, 1, and 10 km

radiation could not have traversed far through the atmosphere so the target is at a close range. If the intensity of the higher band is small compared to the intensity of the lower band, the source must be at a long range.

To compare several source spectra, a specific spectrum is represented as a point on a set of coordinate axes whose values are the intensities in each frequency band. Other spectra are likewise plotted, and if all the spectra are similar then the points should cluster. Distributions are formed by signals that represent sources of the same range.

The frequencies used in the band comparisons are

adjusted to provide maximum separation between each range distribution. Once optimum separation is obtained, ranging algorithms are determined based on the statistical quantities that define the distributions.

#### Assumptions and Limitations

LOWTRAN is a computer code that predicts the transmittance of the atmosphere. To obtain a prediction, a specific atmospheric model must be assumed. The path profile, including source and sensor altitudes, must also be specified. In this analysis, only three specific models representing mid latitude summer, mid latitude winter, and the 1962 U.S. Standard were used. In addition, the path profile was restricted to sea level altitudes for both source and sensor. It would be an inordinate task to attempt an analysis for all model and path profiles. However, the results are based on the absorption from  $\text{CO}_2$  in the atmosphere, and the concentration of  $\text{CO}_2$  is relatively independent of input conditions (Ref 3: V,102-103).

When integrating spectral intensities to obtain a total band intensity, Simpson's Rule will be used with  $5 \text{ cm}^{-1}$  increments. Although the resolution of current spectrometers is better than this, the LOWTRAN transmittance can only be calculated in  $5 \text{ cm}^{-1}$  increments. The LOWTRAN transmittance is actually an average over a  $20 \text{ cm}^{-1}$  band. The resolution of the analysis is therefore limited by LOWTRAN.

The ranging algorithm that will be determined is based on a statistical representation of all sources at one particular range. However, only nine source spectra were available to generate the statistical distributions. The spectra were representative of several types of sources, and it is assumed that the distributions are representative of those that would form if all sources could be analyzed.



## II. Infrared Signatures

### Source Types

There are numerous ways to classify sources of electromagnetic radiation. Most classification schemes rely on the spectral, temporal, or spatial properties of the source to determine its category. In order to predict range by analyzing atmospheric effects, the spectral properties of sources are the most important.

In general, a source can be spectrally categorized as a blackbody, greybody, or selective radiator. A blackbody can be defined as a perfect radiator, or one that radiates the maximum number of photons that any body in thermodynamic equilibrium at the same temperature can radiate (Ref 3:I,2). Other sources are compared to blackbodies by a quantity called emissivity. Emissivity  $\epsilon$  is defined as the ratio of the exitance of a given source to that of a blackbody (Ref 3:I,28):

$$\epsilon(\nu) = \frac{M(\nu, T)}{M_{BB}(\nu, T)} \quad (1)$$

where

$M(\nu, T)$  = spectral exitance of a source at temperature of T

$M_{BB}(\nu, T)$  = spectral exitance of a blackbody at same temperature

A source whose emissivity is a constant independent of wavelength is a greybody, while sources whose

emissivity is a function of wavelength are called selective radiators. In many instances, selective radiators have emissivity functions that cannot be easily represented analytically. Theoretical model calculations can produce tabulated spectral values, but the spectral signature of these sources is best represented by measured results.

Blackbody Sources. When a cavity is an isothermal enclosure at a temperature  $T$ , a small hole in the enclosure will emit blackbody radiation whose spectral exitance can be calculated from Planck's Law (Ref 2:126):

$$M_{BB}(\nu, T) = \frac{C_1 \nu^3}{\exp(C_2 \nu/T) - 1} \quad [W/cm^2-cm^{-1}] \quad (2)$$

where

$\nu$  = wavenumber in  $cm^{-1}$

$C_1 = 2 \pi h c^2 = 3.74 \times 10^{-12} W-cm^2$

$C_2 = (hc/k) = 1.439 cm-K$

Here,  $c$  is the velocity of light,  $h$  is Planck's constant, and  $k$  is Boltzmann's constant.

The spectra for several blackbody radiators are shown in Figure 2. If the temperature of a blackbody source is known, these spectra can be used to estimate the spectral band over which a sensor should operate to detect the source.

When comparing actual sources to blackbody sources, similar units must be used. The available source files are recorded in units of radiant intensity. Assuming a small

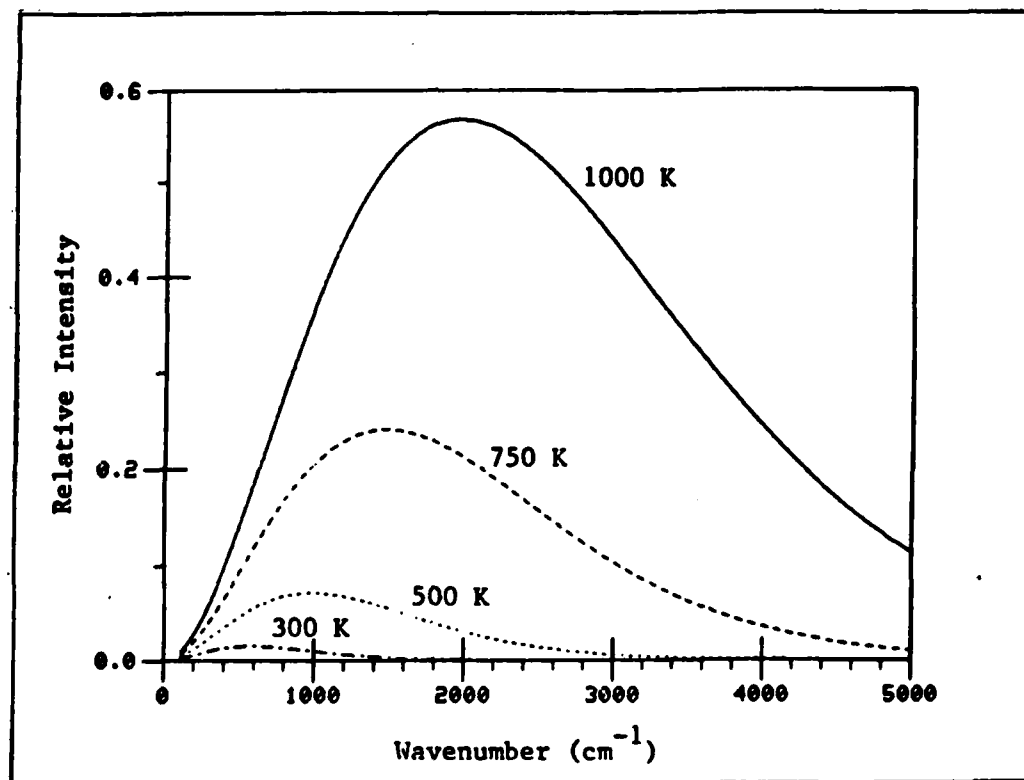


Figure 2. Intensity of Blackbodies at Several Temperatures

field-of-view detector and normal incidence, a point source approximation can be used so that the spectral intensity can be calculated from the spectral exitance by:

$$I_e(\nu) = (A/\pi) M_e(\nu) \quad [W/(sr\text{-}cm^{-1})] \quad (3)$$

where

$I_e(\nu)$  = spectral radiant intensity at the source

$A$  = area of source

To remove the spectral dependence, the spectral intensity is integrated over the spectral bandwidth of the detector:

$$I_e = \int_{\nu_1}^{\nu_2} I_e(\nu) d\nu \quad [W/sr] \quad (4)$$

where

$\nu_1$  = lower wavenumber of bandwidth

$\nu_2$  = upper wavenumber of bandwidth

Selective Radiators. Because of their applicability to infrared ranging, selective radiators resembling aircraft jet engines will be used. Aircraft have special IR signatures resulting from the volume of hot gases emitted by the engine exhaust. Missiles, flares, and high-temperature industrial smokestacks also exhaust hot gases and their spectra therefore resemble that of aircraft. An example of a missile spectrum is shown in Figure 3. The radiation resulting from the vibrational transitions of  $CO_2$  and  $H_2O$  are apparent between  $2000-2500 \text{ cm}^{-1}$  and between  $3000-4000 \text{ cm}^{-1}$ . If the spectral resolution of the detector is sufficient, the fine structure representing transitions between various rotational energy states of the molecules composing the exhaust can also be seen.

For hydrocarbon fuels, the exhaust consists mainly of  $H_2O$  vapor and  $CO_2$ . Because of these, radiation is most intense around  $2300 \text{ cm}^{-1}$  and around  $3700 \text{ cm}^{-1}$ . However, the atmosphere is also composed of  $H_2O$  and  $CO_2$  and is highly absorbent in these spectral bands. Since the gases are hotter than the atmosphere, gas molecules are excited to

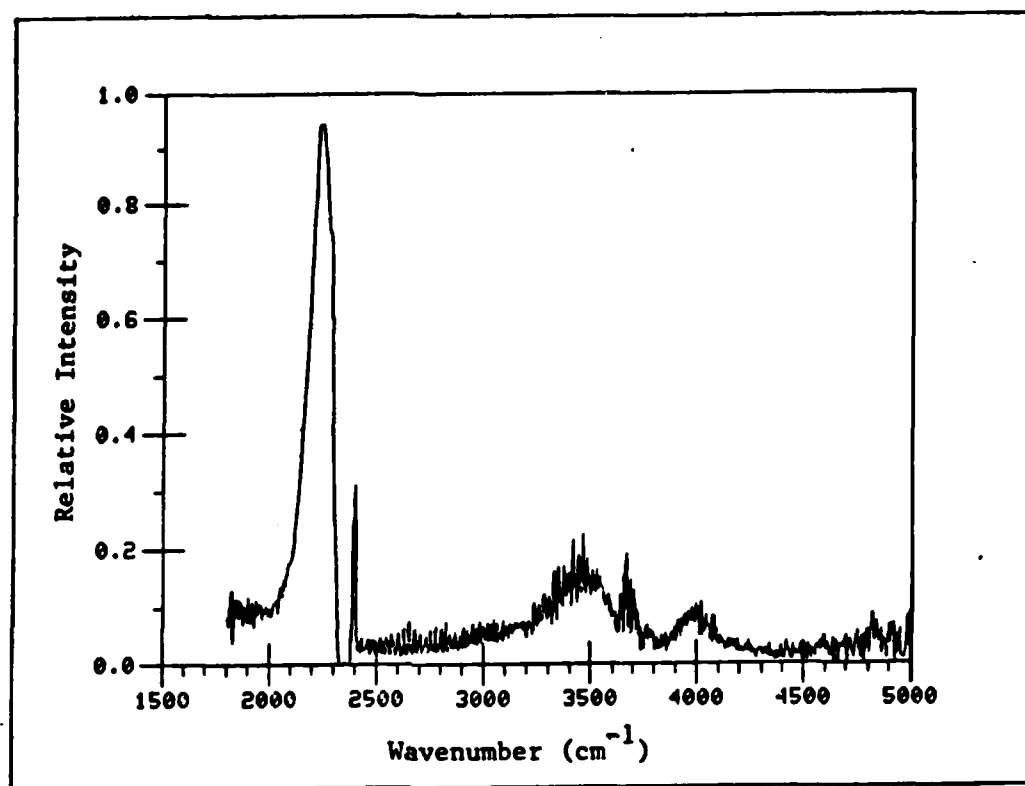


Figure 3. Typical Missile Spectrum (ARI #003)

higher rotational energy levels than the atmospheric molecules. As the hot gas molecules decay to the ground state, they radiate at frequencies that are outside of the strong atmospheric absorption, and the radiation propagates with much less attenuation (Ref 3:II,76-79). This effect causes the apparent lack of radiation in the band between 2225 and 2375  $\text{cm}^{-1}$ . The peak of radiation remaining near 2200  $\text{cm}^{-1}$  is called the red spike while the peak near 2400  $\text{cm}^{-1}$  is called the blue spike. If an aircraft jet engine is running in afterburner, the higher temperature causes more transitions outside of the atmospheric absorption region to occur,

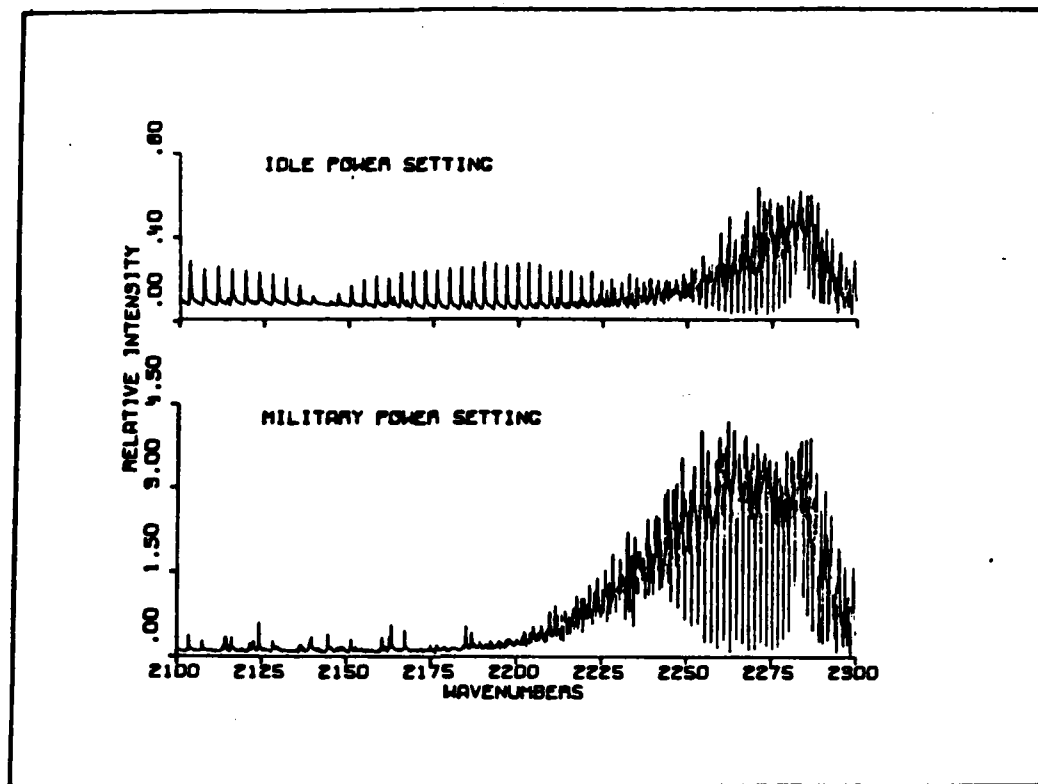


Figure 4. Aircraft Spectrum at Different Power Settings

and the red spike becomes very wide. Because the blue spike is near a bandhead, its width remains relatively constant. A comparison of the exhaust spectra for aircraft at idle and military power is shown in Figure 4. The radiation band is obviously wider when the engine is in military power.

In addition to the selective radiation caused by molecular transitions, the IR spectrum contains a continuum of radiation caused by blackbody-type sources near the target. The hot tailpipe and outer surfaces of an aircraft, or the smokestack of a refinery flare, all contribute to the overall IR signature.

### Atmospherics

The spectral signature of any radiative source is altered as it propagates through the earth's atmosphere. Radiation is attenuated by scattering and absorption processes that depend upon the frequency of the radiation. The received irradiance is proportional to the initial radiance, the density of the attenuating medium, and the distance traversed (Ref 3:IV,3).

Several practical methods exist for calculating the atmospheric spectral transmittance to accuracies of 5 to 10% (Ref 3:V,3). The LOWTRAN method uses a functional form of the transmittance that is determined by a fit of a specialized curve to a plot of actual data (Ref 3:V,47). The results have been computerized and the FORTRAN code is available from the Air Force Geophysics Laboratory (Ref 1). LOWTRAN is frequently updated and the version used in this analysis is called LOWTRAN 5.

The LOWTRAN code calculates transmittance averaged over  $20 \text{ cm}^{-1}$  intervals in steps of  $5 \text{ cm}^{-1}$  from 350 to  $40,000 \text{ cm}^{-1}$  (Ref 1:14). The 1962 U.S. Standard atmosphere and five seasonal models are provided as input options for running the code. In addition, user-defined or measured data may be inserted to represent any atmospheric conditions.

To represent the irradiance detected by an infrared sensor, computer data files containing the transmittance for an atmospheric model at several ranges were created. The

files are generated only for the frequencies over which the analysis is anticipated. An array that contains the intensity of a source can then be multiplied by the appropriate transmittance in the data file and divided by the square of the range to obtain irradiance at the sensor.

### Background Contributions

In the infrared region of the electromagnetic spectrum, background radiation has a significant effect on the amount of radiation seen by a sensor. Most detection systems are contrast sensors and the primary response generated from a source is due to the contrast within the scene. Any black-body radiation from the background is also sensed and becomes a part of the total measured spectrum. If a target-plus-background spectrum is obtained, the target-only spectrum could be calculated by spectrally subtracting the background-only spectrum. When using this technique, care must be exercised so that the background spectrum is obtained under the same conditions that the composite spectrum was obtained (Ref 4:I,1).

In addition to the steady background radiation, a cluttered background such as clouds or terrain that scatters radiation exhibits an intensity pattern that varies from point to point. A sensor scanning such a background generates a response that appears as noise on the signal. In many applications, this clutter noise limits the detection capabilities of the system (Ref 3:XXI,19-20).



### Computer Files

Two sets of data files designed to be used for spectral discrimination analyses were available from previous contracts. Aerodyne Research Inc. has supplied spectra that are computer generated, and validated through comparison with actual measurements. The Air Force Geophysics Laboratory has provided spectra that are taken from actual field measurements.

ARI Files. The library of spectra obtained from Aerodyne are referred to as ARI files. Although numerous source spectra were available, only nine represented targets that resembled aircraft and missiles. One of these files is measured data from a missile firing, and the remainder are computer simulations of flares typically seen near refineries. Different gas and particle concentrations cause minor variations in the spectra, but all are similar.

Table I is a list of the files that were used with a short description of each. Several of the spectra are plotted in Figure 5. Computer generated files are characterized by no noise noticeable in the areas of low intensity radiation. Except for the missile spectrum, all of the ARI files have no noise associated with the signals. The missile file is actually measured data and not computer generated, so it does have noise associated with the signal.

The range of ARI files is simulated by multiplying each wavenumber by a corresponding LOWTRAN transmittance. Using

Table I  
Aerodyne Research Inc. Files

File name	Temp	Description
ARILIB.003	Unknown	Missile firing
ARILIB.015	1800 K	Gas burnoff flare
ARILIB.017	1800 K	Gas burnoff flare
ARILIB.019	1800 K	Gas burnoff flare
ARILIB.035	1600 K	Arc flare
ARILIB.050	1800 K	Gas burnoff flare
ARILIB.052	1800 K	Gas burnoff flare
ARILIB.053	1800 K	Gas burnoff flare
ARILIB.054	1800 K	Gas burnoff flare

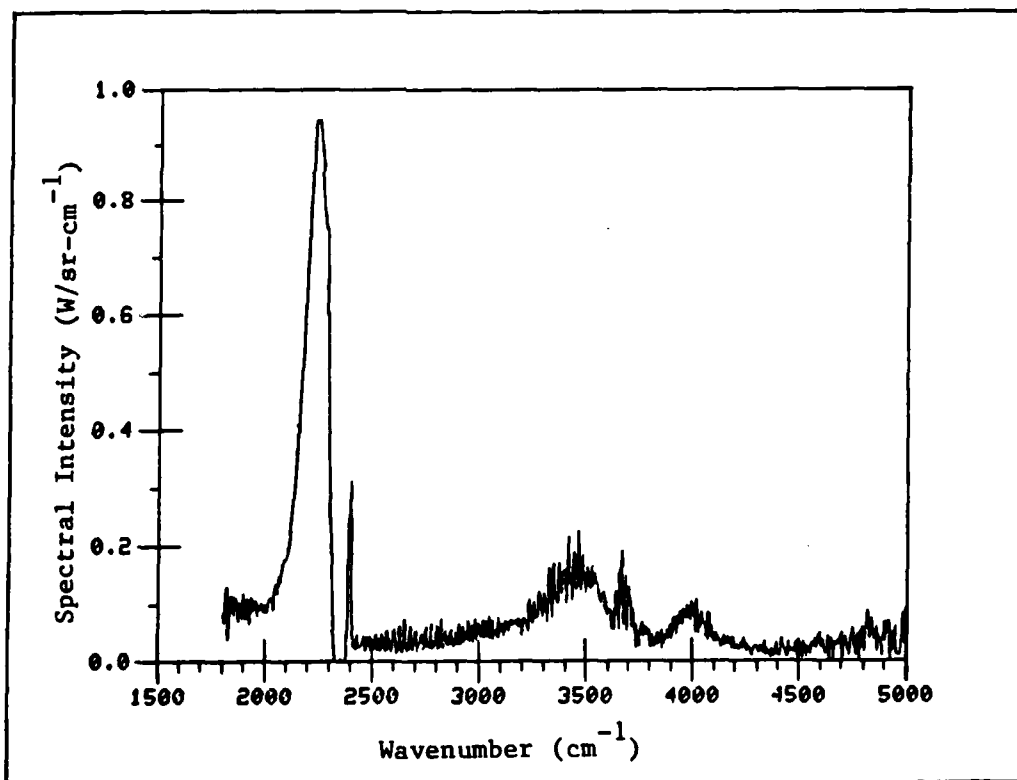


Figure 5a. ARI Missile Spectrum (ARI #003)

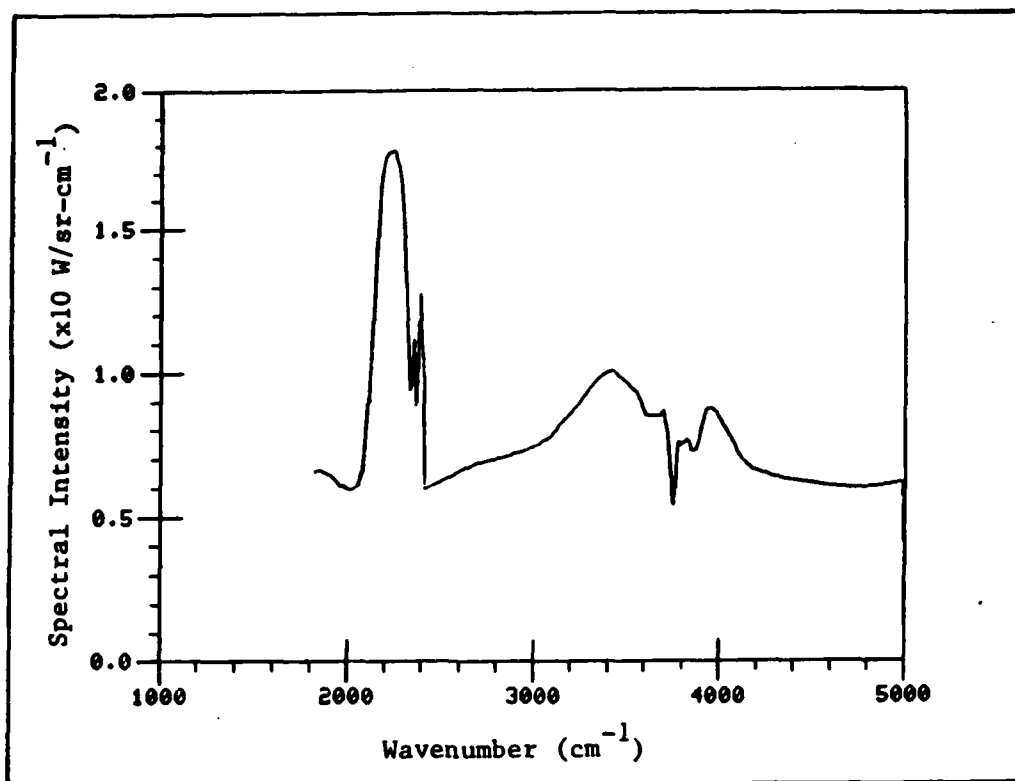


Figure 5b. ARI Flare Spectrum (#017)

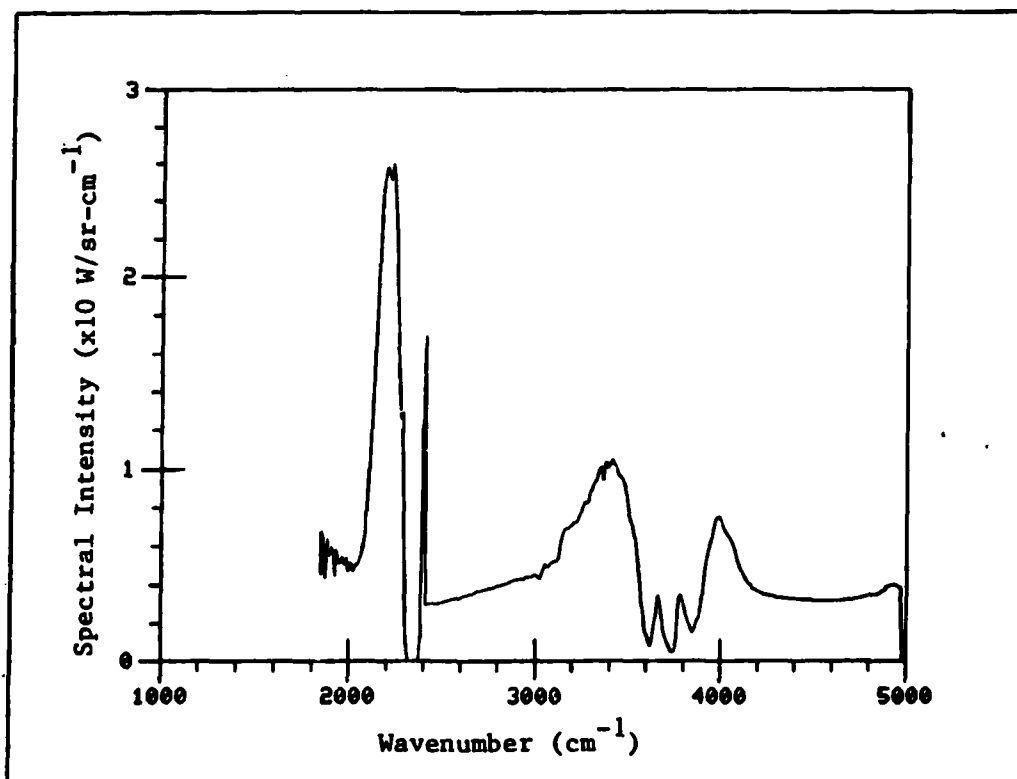


Figure 5c. ARI Flare Spectrum (#050)

this method, sources representing several IR targets can be simulated with different atmospheric conditions and at different ranges.

AFG Files. Actual measured spectra obtained from the Air Force Geophysics Laboratory are referred to as AFG files. These measurements were obtained from an aircraft flying over industrial areas of the South and Midwest in June 1978 with a one degree field-of-view spectrometer (Ref 5:100). The field-of-view projection is larger than the diameter of most of the sources, so the original spectra contain contributions from the backgrounds. Background spectra near the targets were also recorded, and were subtracted from the target spectra to provide source-only spectra. Because the ranges and background radiances are somewhat uncertain, the spectra have associated uncertainties of perhaps  $\pm 25\%$  (Ref 5:106). Unfortunately, the ranges of all sources are only between 2.6 and 4.7 km.

Several of the sources do not represent hot gas sources, but are more characteristic of cool gases and greybody emitters. Cool gases are sources that have only a small amount of radiation that is emitted beyond the atmospheric absorption band ( $<1000$  K); hot gases emit well beyond the atmospheric absorption band. The actual type of these sources falls into one of the following categories:

- 1) Coke oven/blast furnace
- 2) Smoke and flare stacks

Table II  
Air Force Geophysics Lab Files

File name	Type	Temp	Location	Range
AFGLIB.001	Hot Ore	819 K	Indiana	3.5
AFGLIB.002	Hot Slag	845 K	Indiana	3.5
AFGLIB.003	Coke Oven	496 K	Indiana	3.9
AFGLIB.004	Flare Stack	None	Indiana	4.7
AFGLIB.005	Mill Stacks	600 K	Indiana	4.4
AFGLIB.006	Blast Furn.	600 K	Michigan	4.7
AFGLIB.007	Coke Oven	481 K	Michigan	2.8
AFGLIB.008	Stacks	800 K	Michigan	4.4
AFGLIB.009	Hot Metal	800 K	Michigan	3.2
AFGLIB.010	Stacks	600 K	Michigan	3.2
AFGLIB.011	Flare Stack	1700 K	Kentucky	3.3
AFGLIB.012	Hot Bldgs.	500 K	Kentucky	2.9
AFGLIB.013	Stacks	400 K	Alabama	2.9
AFGLIB.014	Hot Bldgs.	600 K	Alabama	3.1
AFGLIB.015	Hot Metal	1500 K	Alabama	2.6
AFGLIB.016	Hot Bldgs	575 K	Kentucky	2.7

3) Hot metals and ore

4) Hot buildings

One of each of these types of source spectra is plotted in Figure 6, and a list of all the files is given in Table II. The temperature listed in Table II is the temperature of a blackbody source whose spectrum closest resembles that of the actual source. It is not necessarily the actual source temperature because the source's spatial distribution is not considered. Because the spectrometer had a high resolution, the fine structure of the emission is noticeable in Figure 6. This will later cause problems because the ARI

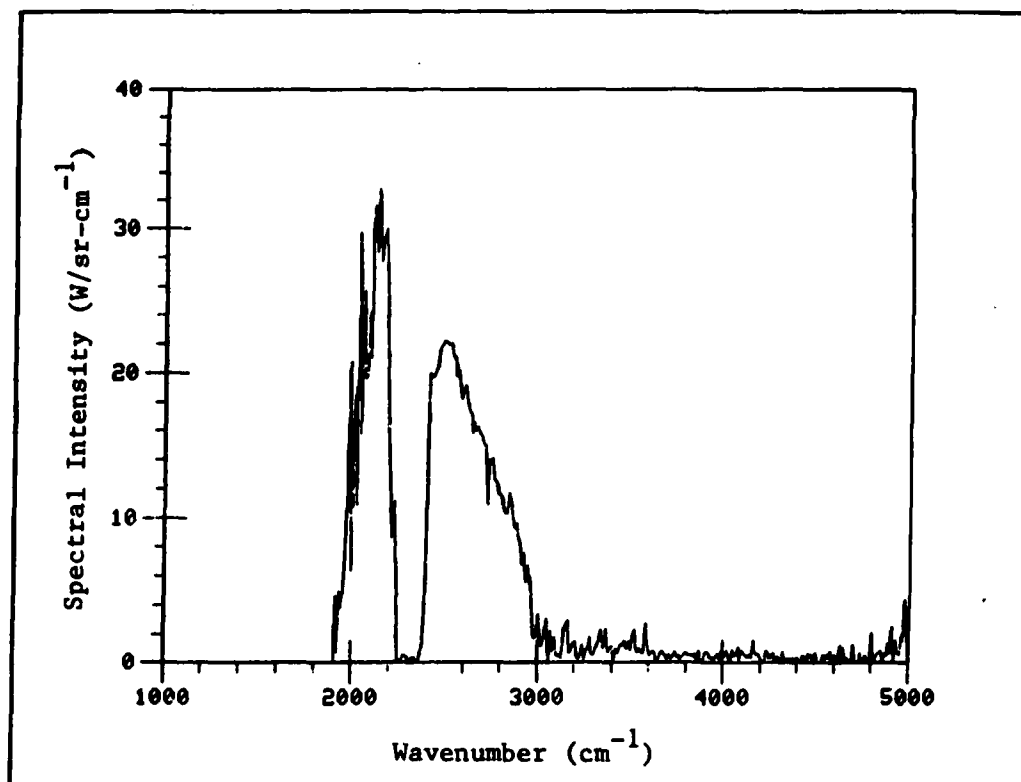


Fig 6a. AFG Coke Oven Spectrum (#003)

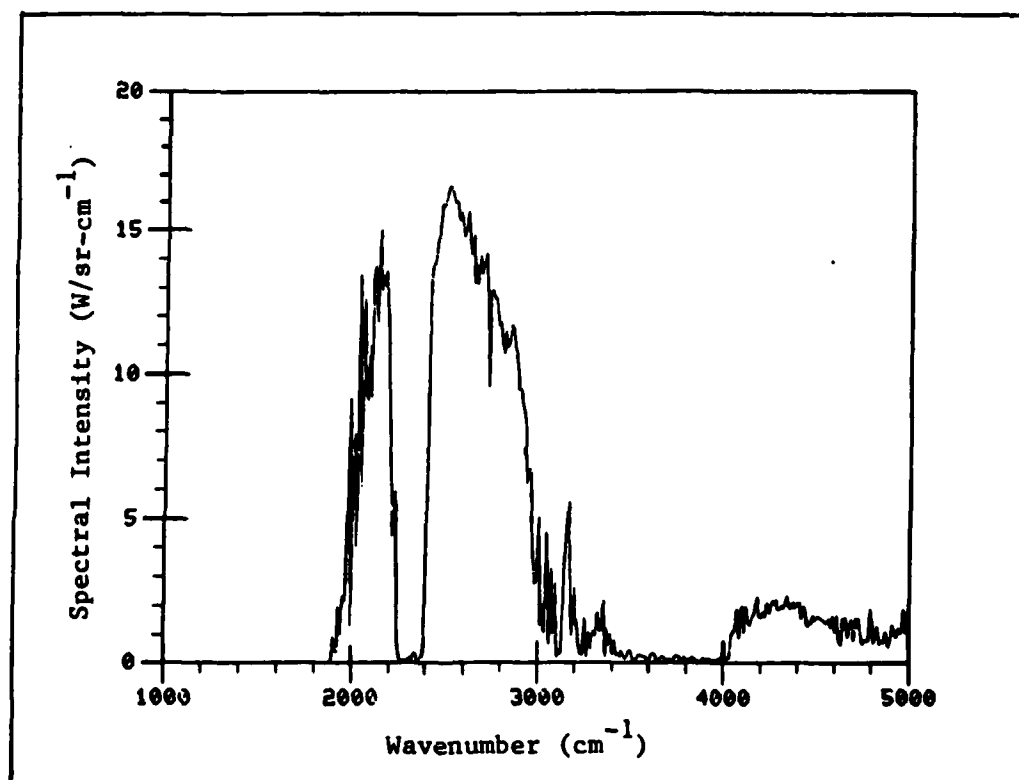


Fig 6b. AFG Hot Metal Spectrum (#009)

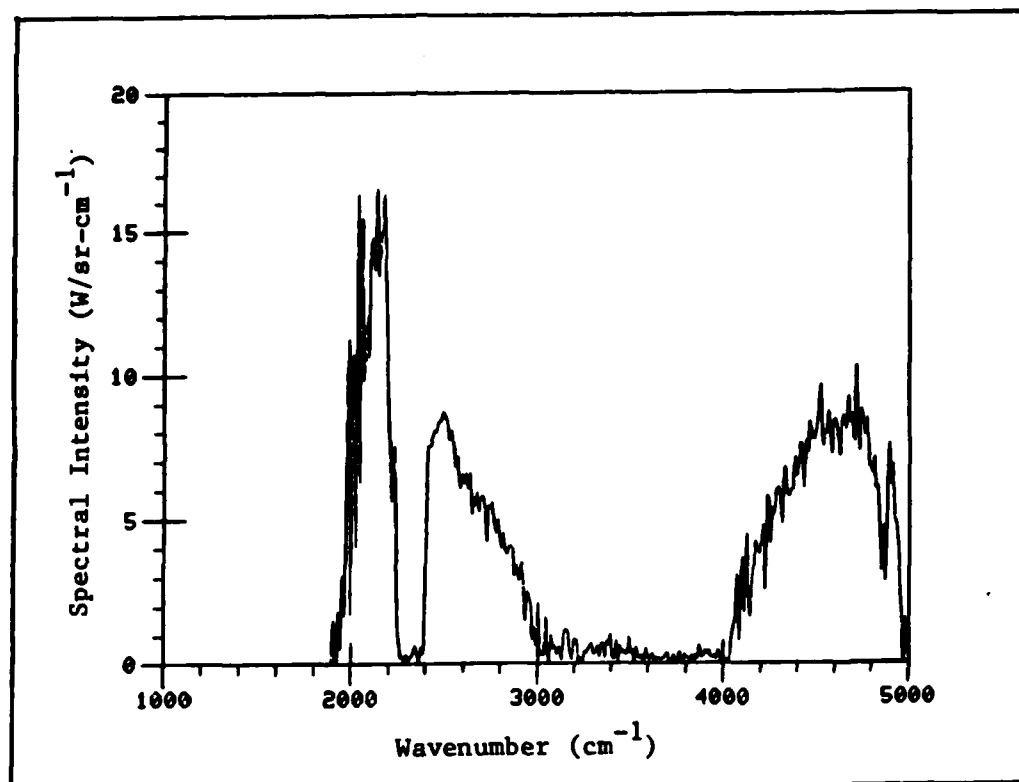


Fig 6c. AFG Smoke Stack Spectrum (#010)

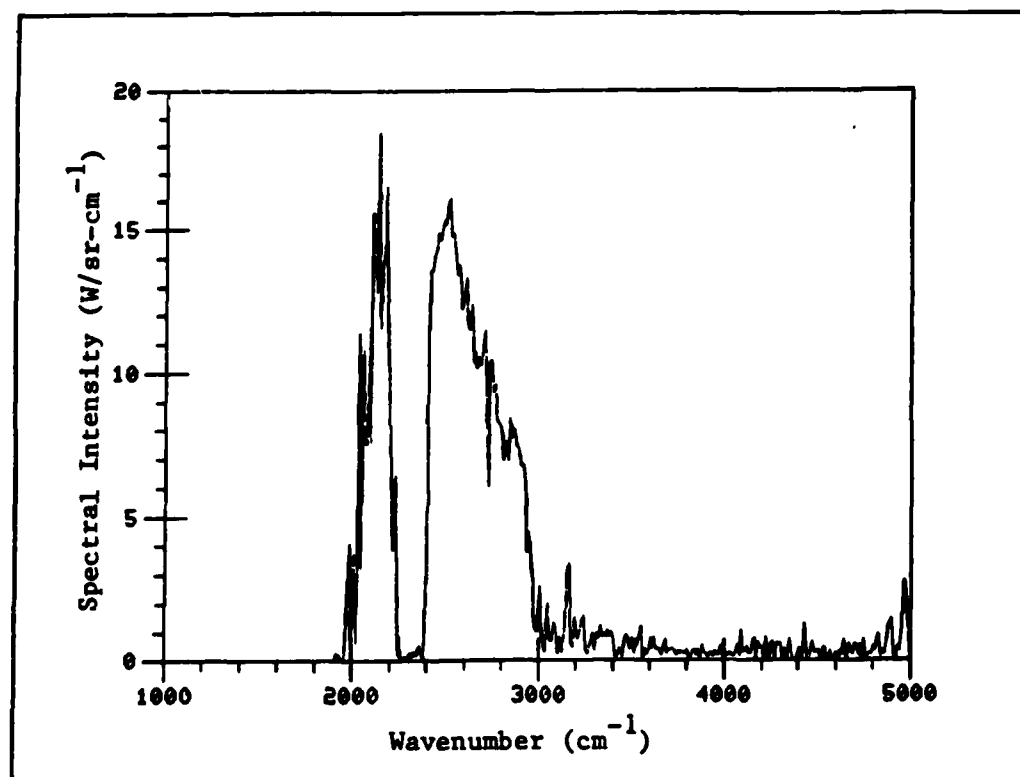


Fig 6d. AFG Hot Building Spectrum (#014)

files multiplied by LOWTRAN generate low resolution spectra in which none of the atmospheric fine structure is present.

Because of their security classification, actual sources representing aircraft and missile signatures could not be obtained. However, the AFG files do represent actual measured results and are therefore used to test the ranging algorithm. Unfortunately, the range of these sources only varies from 2.6 to 4.7 km, and thus they provide only a limited check of the algorithm.



### III. Spectral Discrimination

#### Pattern Recognition

Spectral pattern recognition is the process of identifying a class of events by analyzing the spectrum that has been produced or influenced by the event (Ref 6:2699). Ideally the process will correctly identify all of the desired events and reject all background, interference, and noise.

The received spectrum of any source may be represented by  $N$  spectral amplitudes  $(S_1, S_2, \dots, S_N)$  at the corresponding  $N$  different wavelengths or colors. The spectrum can then be represented in an  $N$ -dimensional color space by the coordinates  $(S_1, S_2, \dots, S_N)$  along  $N$  orthogonal axes. A set of spectra from one class of events can be represented by a group of points in the color space. Assuming that the spectra from the class are similar, the points will form a cluster.

If a different class is represented by the same scheme, two clusters will form in color space. If little or no overlap exists between the two clusters, the classes can be accurately distinguished. Figure 7 shows an example of two classes of events plotted in a two-dimensional color space.

Because the spectrum of any event or class of events is not unique, pattern recognition becomes a statistical problem. To simplify the statistical calculations, normal

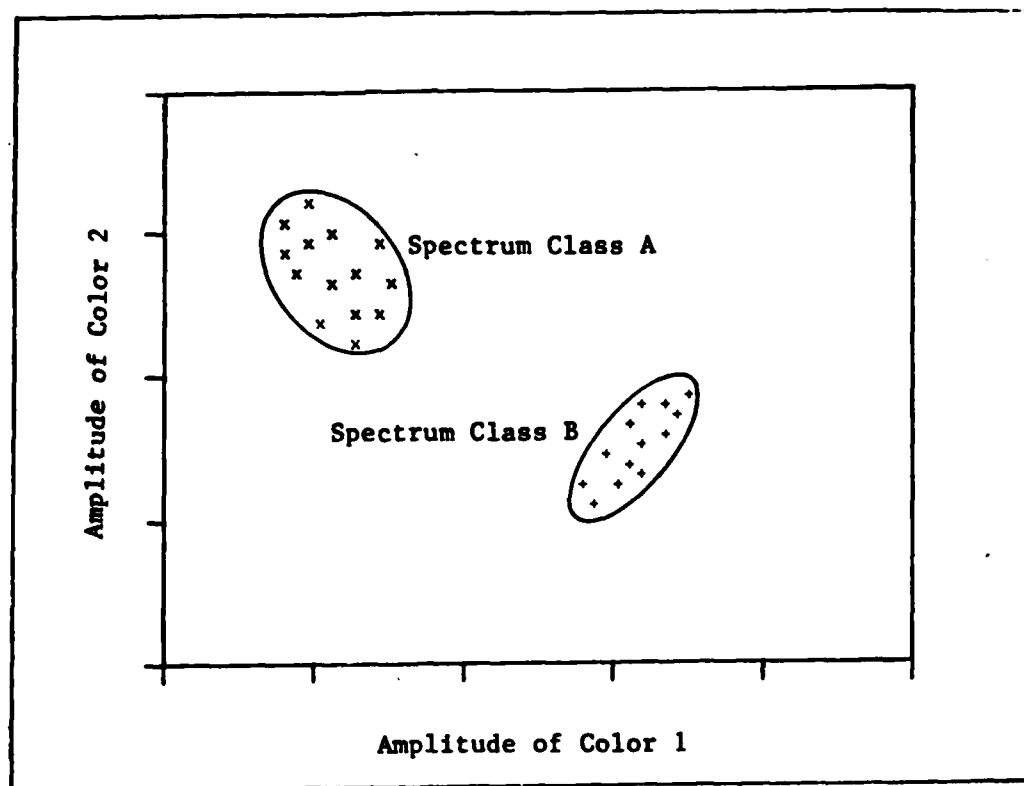


Figure 7. Spectral Classes in Color Space (Ref 6)

Gaussian statistics are assumed. Although the data obtained from infrared spectra does not entirely support normal statistics, it has been shown that a decision rule based on normal distributions performs nearly as well as rules derived from the empirical frequency of the data (Ref 7:162). By using normal statistics, calculations are simplified and the distributions can be uniquely characterized by their mean vector and covariance matrix (Ref 8:22).

Distributions in color space can be partitioned into separate regions called decision regions. One decision region must be associated with each class of events or

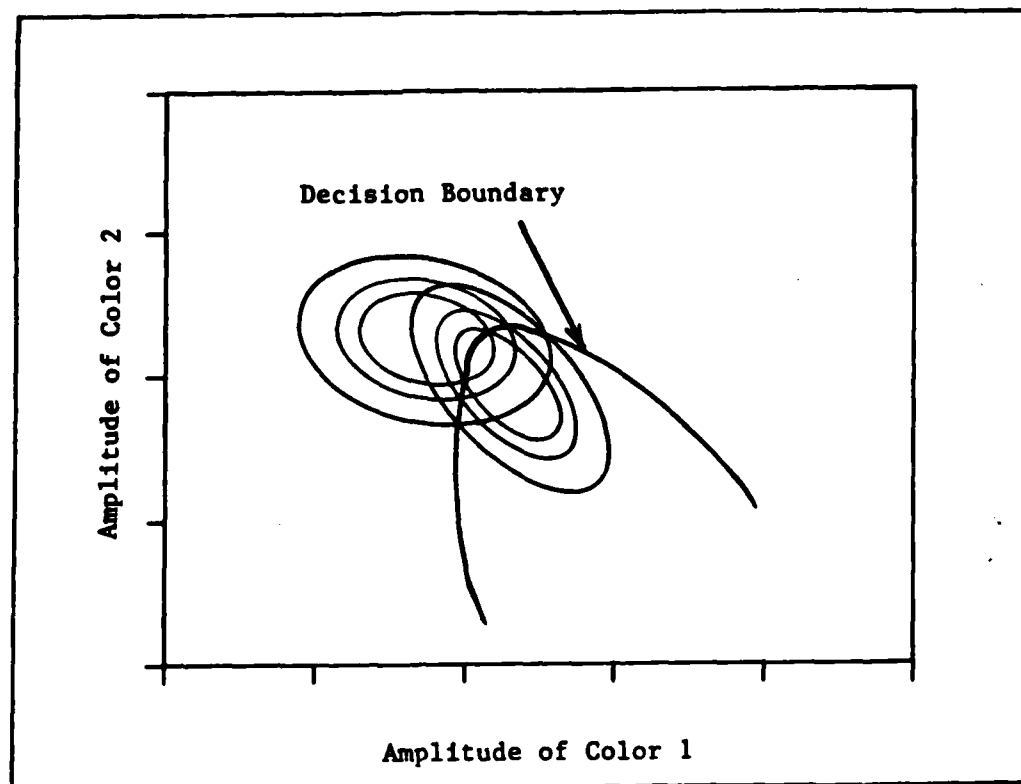


Figure 8. Decision Boundaries for Normal Distributions  
(Ref 8:53)

cluster, and should contain most of the points for that cluster. Any new point from an unclassified source can be assigned according to the decision region into which it falls.

There several methods available for determining the decision boundaries. Using a maximum likelihood criteria (Ref 8:53), construction of the decision regions is easily visualized by plotting contours of equal density as in Figure 8. The decision function that separates the two distributions is defined by the intersections of contours of equal density. For Gaussian distributions, the contours are

ellipses and the decision functions are quadratic. When the two distributions have equal covariance, the decision functions become linear. A method to calculate the slope of the line separating normal distributions of equal covariance is discussed in Appendix A.

### Gaussian Statistics

A vector whose components are random variables is called a random vector. A random vector is fully characterized by its distribution or density function. Often these functions cannot be easily determined, or are too complex to be of practical use. It is therefore convenient to use less accurate but more computable density functions to represent some types of distributions.

When using Gaussian statistics, the density function of a multivariate distribution is completely represented by its mean or expected vector and its covariance matrix. The mean vector of a random vector  $\bar{X}$  is defined as (Ref 8:16):

$$\bar{M} = E[\bar{X}] = \int_s \bar{X} p(\bar{X}) d\bar{X} \quad (5)$$

where

$E[\bar{X}]$  = expectation value of vector  $\bar{X}$

$p(\bar{X})$  = density function of  $\bar{X}$

$s$  = all  $\bar{X}$  space

The covariance matrix  $\underline{C}$  is defined by (Ref 8:17;10:34):

$$\underline{C} = E[(\bar{X}-\bar{M})^T(\bar{X}-\bar{M})] \quad (6a)$$

$$= \int_s (\bar{X}-\bar{M})^T(\bar{X}-\bar{M}) p(\bar{X}) d\bar{X} \quad (6b)$$

where T represents the transpose of a vector. The diagonal components of this matrix are the variances of individual random variables and the off-diagonal components are the covariances of the two corresponding variables.

When only a finite number n of spectra are available to characterize a distribution, the mean vector is calculated by (Ref 9:236)

$$\bar{M} = (1/n) \sum_n \bar{X} \quad (7)$$

The covariance matrix is estimated by

$$\underline{C} = [1/(n-1)] \sum_n (\bar{X}-\bar{M})^T(\bar{X}-\bar{M}) \quad (8)$$

Sometimes it is convenient to normalize covariance matrices by converting the individual covariance terms to correlation coefficients  $r_{ij}$  as

$$r_{ij} = \frac{c_{ij}}{\sigma_{ii} \sigma_{jj}} \quad (9)$$

where

$c_{ij}$  = matrix element of  $\underline{C}$

$\sigma_{ii}$  = standard deviation of band i

Because the variance is the square of the standard deviation, the diagonal elements of the correlation matrix  $\underline{R}$

are unity.

When using Gaussian statistics, the distribution function  $p(\bar{X})$  is given in terms of the mean vector and covariance matrix by (Ref 10:35):

$$p(\bar{X}) = (2\pi)^{-d/2} |\underline{C}|^{-1/2} \exp[\frac{1}{2}(\bar{X}-\bar{M})^T \underline{C}^{-1}(\bar{X}-\bar{M})] \quad (10)$$

where

$d$  = dimension of  $\bar{X}$

$|\underline{C}|$  = determinant of  $\underline{C}$

$\underline{C}^{-1}$  = inverse of  $\underline{C}$

### Cluster Discrimination

To reduce the probability of an erroneous classification, the separation between distributions must be large. The Bhattacharyya distance is one measure of this separation and is defined by (Ref 8:268):

$$B = -\ln \int_s [p_1(\bar{X}) p_2(\bar{X})]^{\frac{1}{2}} d\bar{X} \quad (11)$$

By assuming normal statistics, the Bhattacharyya distance can be written as (Ref 8:268):

$$B = (1/16)(\bar{M}_1 - \bar{M}_2)^T (\underline{C}_1 + \underline{C}_2)^{-1} (\bar{M}_1 - \bar{M}_2) + \frac{1}{2} \ln [\frac{1}{2}(\underline{C}_1 + \underline{C}_2) |\underline{C}_1|^{-\frac{1}{2}} |\underline{C}_2|^{-\frac{1}{2}}] \quad (12)$$

This distance is zero when two distributions are identical, and is infinite when there is no overlap.

The Bhattacharyya distance is the sum of two terms.

The first term in the equation is called the Mahalanobis distance and is essentially the square of the distance between the means of each distribution. The distance is measured relative to the average of the covariances. The second term is an added separation arising from different covariances. If the means of the distributions are equal, the Mahalanobis distance vanishes, but there may still be separation from the second term. If the covariances are equal, the second term vanishes and the only separation is from the difference of the means.

Using a maximum likelihood criterion, the probability of an erroneous classification can be approximated in terms of the Bhattacharyya by the expression (Ref 11)

$$E = (2B^2\pi)^{-\frac{1}{2}}\exp(-B^2) \quad (13)$$

Error for a Bhattacharyya distance of 1.0 is calculated to be approximately 0.147 while a Bhattacharyya distance of 2.0 results in an error of only 0.004. For Gaussian statistics, a Bhattacharyya separation of 2.0 therefore represents small overlap between two distributions.

In some applications of pattern recognition, it is practical to use only a few wavelengths or spectral bands when analysing source spectra. Optimum bands are found by changing the combination of wavelengths until the Bhattacharyya distance between distributions in color space is maximized. The least number of bands is sought that still

permits adequate separation between distributions.

### Intensity Normalization

The intensity of any source has a direct effect on the location of the point plotted in color space. Bright sources are located farther from the origin than dim sources of the same class because the spectral amplitude of all bands will be greater for the bright source. When trying to discriminate certain classes of events by spectral pattern recognition, it is sometimes desirable to obtain results that are independent of source intensity.

In the development of spectral representation using color space, a point representing one spectrum of a class of events was plotted using rectangular coordinates  $(S_1, S_2, \dots, S_N)$  defined by the spectral amplitude in  $N$  bands. Using only three bands for comparison, any point in color space can also be represented with spherical coordinates  $(\rho, \theta, \phi)$  by (Ref 12:385):

$$\rho = (S_1^2 + S_2^2 + S_3^2)^{\frac{1}{2}} \quad (14a)$$

$$\theta = \arctan(S_2/S_1) \quad (14b)$$

$$\phi = \arccos[(S_3)/(S_1^2 + S_2^2 + S_3^2)^{\frac{1}{2}}] \quad (14c)$$

Using spherical coordinates, the intensity of a source is indicated by the magnitude of  $\rho$ , and the relative intensities among the three bands are given by the values of  $\theta$  and  $\phi$ . If it is desirable to have a color space representation that is independent of source intensity, the point



can be plotted using a two-dimensional coordinate system whose axes are represented in rectangular coordinates by the values of  $\theta$  and  $\phi$ .

If only two bands are used in the color space representation, the point can similarly be located using plane polar coordinates where (Ref 12:378):

$$r = (S_1^2 + S_2^2)^{\frac{1}{2}} \quad (15a)$$

$$\theta = \arctan(S_2/S_1) \quad (15b)$$

If a color space representation independent of source intensity is required, the two-dimensional point can be represented in only one dimension defined by the value of  $\theta$ . In addition to removing the dependence of the distributions on source intensities, this "reduced" color space representation simplifies the calculation of the statistical measures by reducing the vectors and matrices by one dimension.

#### IV. Spectral Optimization

##### Band Selection

It has already been mentioned that blackbody curves are useful to predict the spectral band over which a sensor must operate. In Figure 2, blackbody curves were plotted for several realistic temperatures. Radiation for blackbody sources near 1000 K is most intense between 1000 and 4000  $\text{cm}^{-1}$ .

Actual sources, however, do not emit broadband radiation as blackbodies do. An example of a missile spectrum was plotted in Figure 3. Sensors that are to detect this type of source can be further limited to the regions between 2000 and 2500  $\text{cm}^{-1}$  or 3300 and 3800  $\text{cm}^{-1}$ . Much of this radiation is absorbed by the atmosphere, though. Because the transmittance of the band between 3300 and 3800  $\text{cm}^{-1}$  is lower, and scattered solar radiation is more pronounced, the optimum spectral region is between 2000 and 2500  $\text{cm}^{-1}$ .

To avoid range errors that may be caused by climatic differences, spectral bands should be chosen that minimize the variation in transmittance between different atmospheric models. LOWTRAN transmittance for several models at the same range is plotted in Figure 9. Variations from  $\text{H}_2\text{O}$  vapor become very pronounced below 2175  $\text{cm}^{-1}$ . Wavenumbers below this value will not be used. Transmission in the  $\text{CO}_2$  band between 2275 and 2375  $\text{cm}^{-1}$  is negligible for all

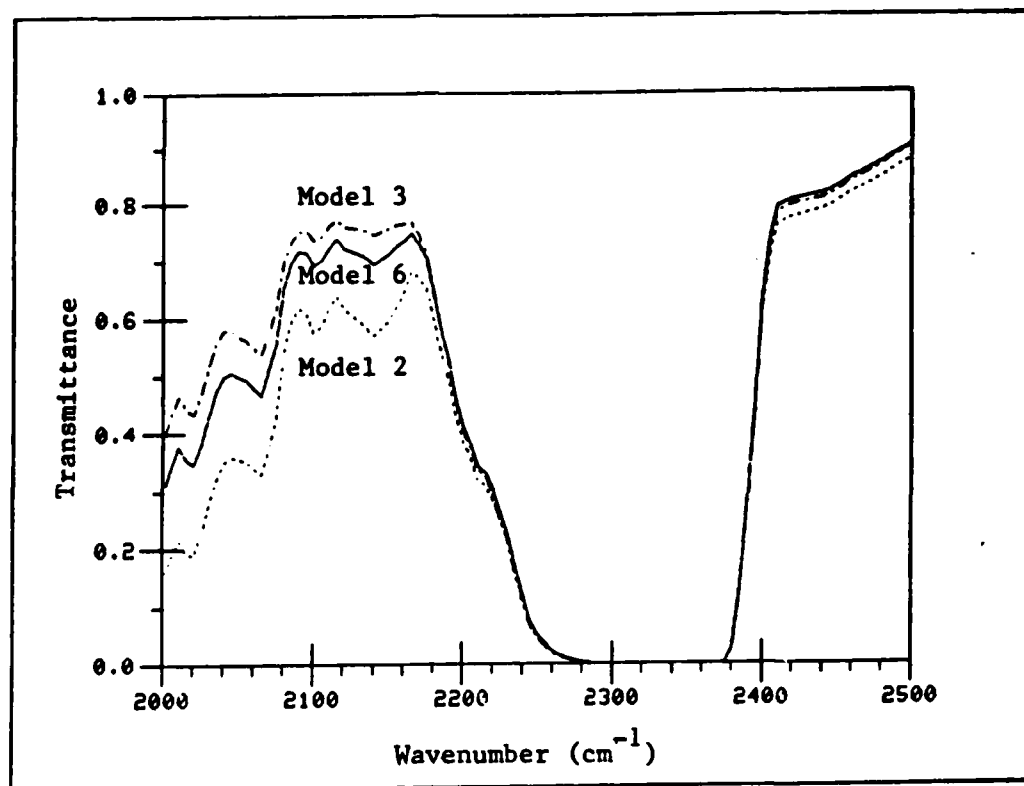


Figure 9. LOWTRAN Model Comparison at 2 km

models, so this band cannot be used either. Above  $2375 \text{ cm}^{-1}$ , a sensor would be detecting a source's blue spike. Because the blue spike is very narrow and source spectra in this region vary considerably, the wavenumbers above  $2375 \text{ cm}^{-1}$  will also be avoided. The only band that remains is between  $2175 \text{ cm}^{-1}$  and  $2275 \text{ cm}^{-1}$ . The atmospheric transmittance at several ranges is plotted in Figure 10 for this spectral region. The regular increase in  $\text{CO}_2$  absorption is the atmospheric effect that will be used to determine the range of a source by examining its spectrum.

One of the limitations of LOWTRAN is the spectral

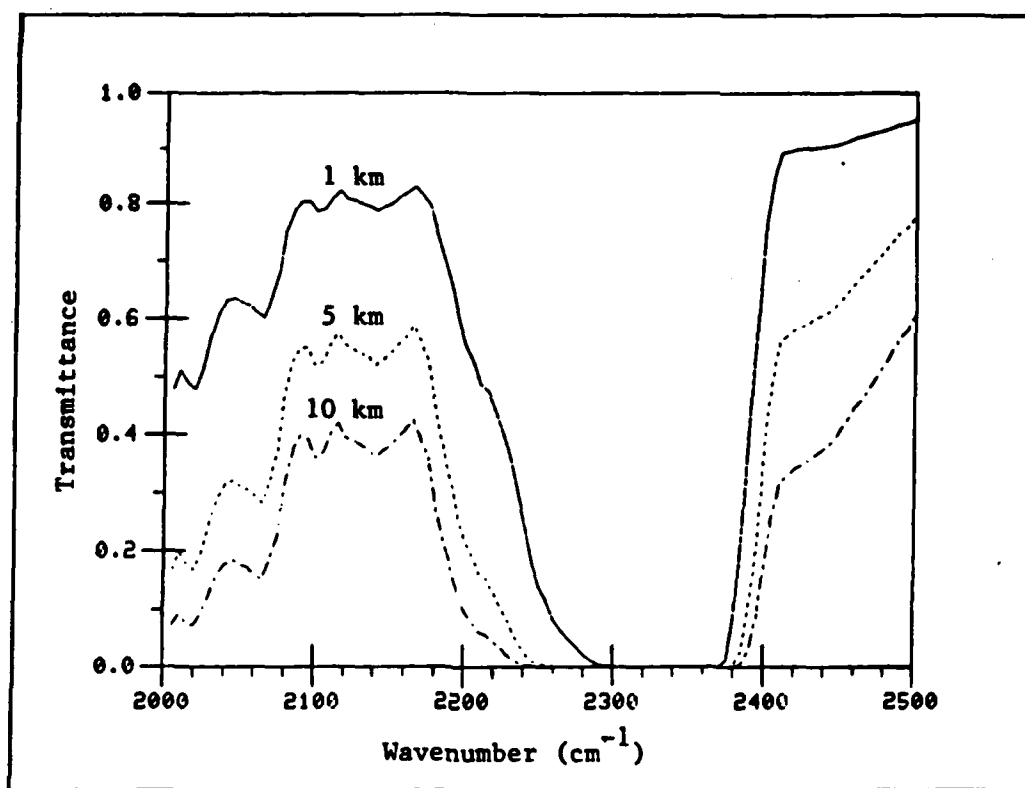


Figure 10. LOWTRAN Range Comparison for Model 6

resolution of  $20 \text{ cm}^{-1}$ . Minimum bandwidths will be restricted to  $25 \text{ cm}^{-1}$  because of this limitation. If smaller bandwidths are required to resolve spectral differences, a more accurate atmospheric model will have to be used for the analysis.

#### Bhattacharyya Measure

The spectral region between  $2175$  and  $2275 \text{ cm}^{-1}$  was divided into four bands as follows:

band 1: $2175\text{--}2200 \text{ cm}^{-1}$	band 2: $2200\text{--}2225 \text{ cm}^{-1}$
band 3: $2225\text{--}2250 \text{ cm}^{-1}$	band 4: $2250\text{--}2275 \text{ cm}^{-1}$

By choosing any combination of these bands, the spectrum of any source can be represented in color space. Initially only two bands were used for comparison, so color space is a two-dimensional coordinate system whose axes are the intensities in each band. To remove the dependence of the color space representation on the intensity of the source, the spectrum was represented in reduced color space. For two bands, reduced color space is one dimension whose value is the arctangent of the ratio of the intensity in the two bands.

The first sources used were blackbody spectra multiplied by LOWTRAN transmittance. Several blackbody functions at temperatures between 500 K and 2000 K were multiplied by three different LOWTRAN models. The models chosen represent midlatitude summer (model 2), midlatitude winter (model 3), and the 1962 U.S. Standard (model 6). Ranges between 2 km and 16 km were calculated. The resulting spectra were then integrated over the selected frequency bands to determine the location of the spectral representation in reduced color space.

All the source combinations for one range form a distribution of points in reduced color space. The mean and covariance matrix for the distribution were calculated. In one dimension, the covariance matrix is simply the square of the standard deviation of the angle  $\theta$ . The distributions for all the ranges used were calculated using this method.

To determine the separation between each range distribution, the Bhattacharyya distance was calculated. Large values for the Bhattacharyya distance mean that the range distributions are well separated. Obviously, the actual distance will depend on the range increment used. Because the Bhattacharyya distance is only used as a comparison between band choices, the range increment is not critical. It does however give an idea of the resolution that may be obtained using this method. If the Bhattacharyya separation between 2 km range distributions is large, then 2 km range resolution may be possible. If there is large overlap between 2 km distributions, there will be large uncertainty as to which distribution an unclassified source should be assigned.

After calculating the Bhattacharyya separation between each range distribution, the band choice was changed and new distributions were formed. Bhattacharyya distances between the new distributions were calculated and compared with the results of the previous bands. The band choice that provides the highest separation between range distributions will provide the best resolution when trying to assign unclassified sources to a specific range.

In Figure 11, the Bhattacharyya distances obtained with several possible band combinations are plotted. Band 4 combinations are not shown because the Bhattacharyya distances obtained were small. The intensity in this band was

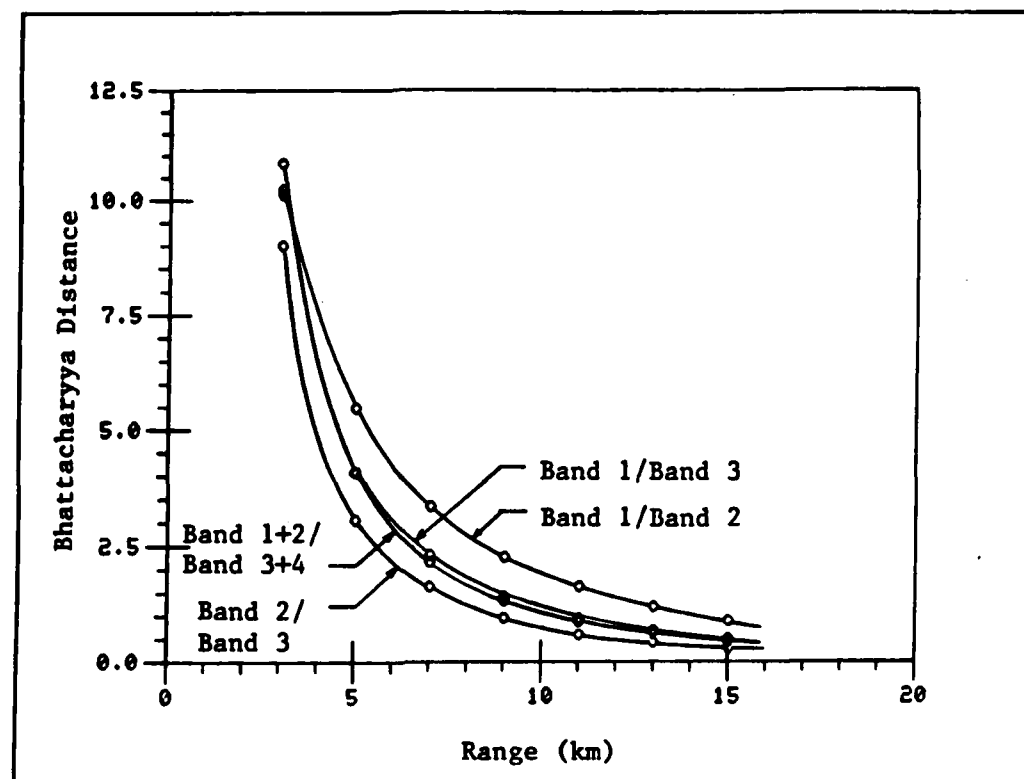


Figure 11. Bhattacharyya Separation for Blackbody Sources Using Two Colors

too low at all ranges to allow sufficient separation between range clusters. At close ranges, the separation is very good for all other band choices. As range increases however, the separation drops rapidly. This is because the intensity of the highest wavenumber band becomes very small due to  $\text{CO}_2$  absorption, and the ratio of the two bands approaches 0. As the ratio approaches 0, so does the angle  $\theta$  that defines the location of the distributions in reduced color space. The range distributions tend to congregate near  $\theta = 0$ , and the Bhattacharyya distances therefore become small.

The optimum bands for blackbody sources is band 1 (2175-2200  $\text{cm}^{-1}$ ) and band 2 (2200-2225  $\text{cm}^{-1}$ ). Bhattacharyya distances between range clusters remains above 2.0 until 10 km using only two colors for comparison. Although actual sources are not well represented by blackbody functions, this analysis has shown that IR signatures can be used to classify sources according to range.

Source files in the ARI library were analysed in the same manner. Because of the number of source files available and the computer time required to read and reduce the data files, LOWTRAN was limited to the 1962 U.S. Standard model atmosphere and 23 km haze visibility. Deviations caused by atmospheric variations are discussed in the results. Again, only two bands were used to begin the analysis.

The Bhattacharyya distances are plotted in Figure 12 for all possible band combinations. The optimum separation is obtained with band 2 (2200-2225  $\text{cm}^{-1}$ ) and band 3 (2225-2250  $\text{cm}^{-1}$ ). With these bands, the Bhattacharyya distance remains above 2.0 only through 5 km. This separation is not sufficient to attempt a ranging algorithm, so three bands for comparison will have to be used.

It should be noted that these bands are at a higher wavenumber than the bands obtained with blackbodies. With blackbodies, it was found that the absorption near the  $\text{CO}_2$  band became too large for higher wavenumber bands. Best



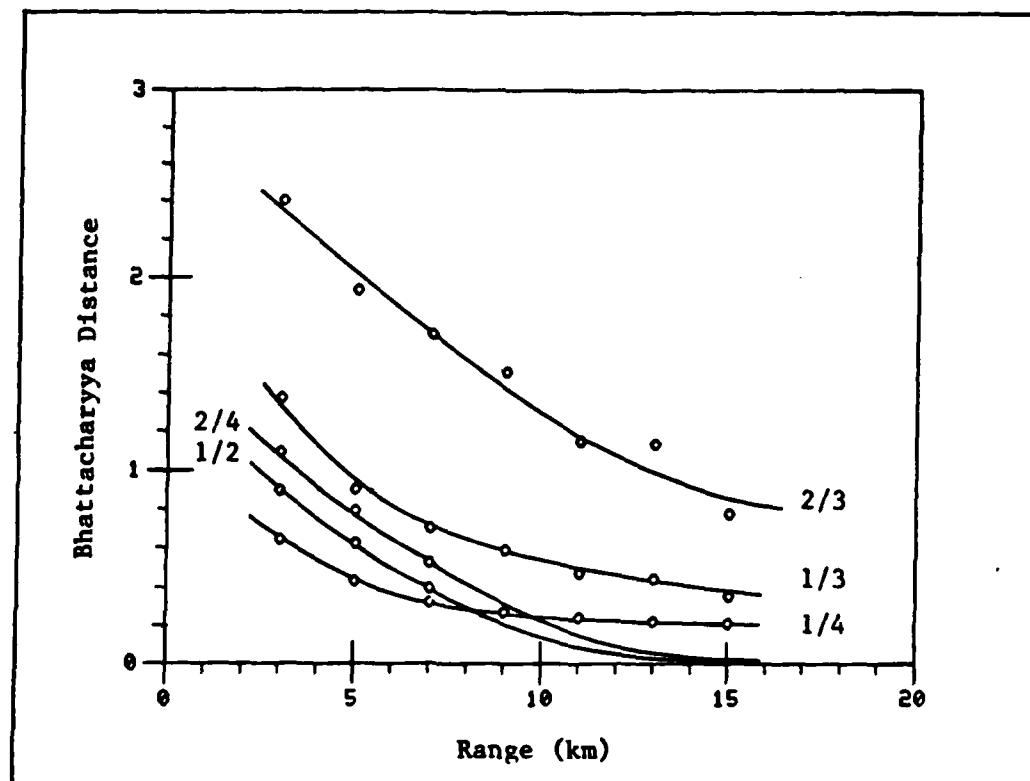


Figure 12. Bhattacharyya Separation for ARI Sources Using Two Colors

results were obtained by choosing bands as far away from the  $\text{CO}_2$  band as possible. With actual sources however, the radiation intensity begins to decrease as the wavenumber moves away from the  $\text{CO}_2$  band. This is typical of cool gas sources, so frequency bands must be chosen adjacent to the  $\text{CO}_2$  band for sources that are cool gas radiators.

Several ARI files that are not listed could not be used because of this problem. The sources represented power plant buildings at a temperature of 400 K, and the spectra resembled cool gases. When the spectral representations of these sources were plotted in reduced color space, the

points did not fall near the proper range distribution. Cool gas sources will therefore not provide accurate range estimates with the algorithm that will be determined.

To improve the Bhattacharyya separation between range distributions, the ARI spectra were analyzed using three bands. The only choice available for the third band was between band 1 and band 4. Because the intensity of band 4 is extremely low at longer ranges, band 1 was chosen as the third band.

The integrated intensity in all three bands was calculated for each ARI source file at ranges between 2 and 18 km. Using three colors, the spectral representation in reduced color space is a point in a two dimensional coordinate system whose axes are the values of the spherical coordinate angles  $\theta$  and  $\phi$ . In Appendix B, the value of each band intensity, and the values of  $\theta$  and  $\phi$ , are tabulated for all sources at all ranges. In addition, the mean and standard deviation of  $\theta$  and  $\phi$  are given to define the Gaussian distribution parameters for each range cluster.

In Figure 13, the spectral representations for all sources are plotted in reduced color space, and ellipses are drawn around points representing sources at the same range. By looking at the graph, it is obvious that there is good separation between all of the range clusters, even at longer ranges. The Bhattacharyya distances between the distributions are plotted in Figure 14. Separation increases with

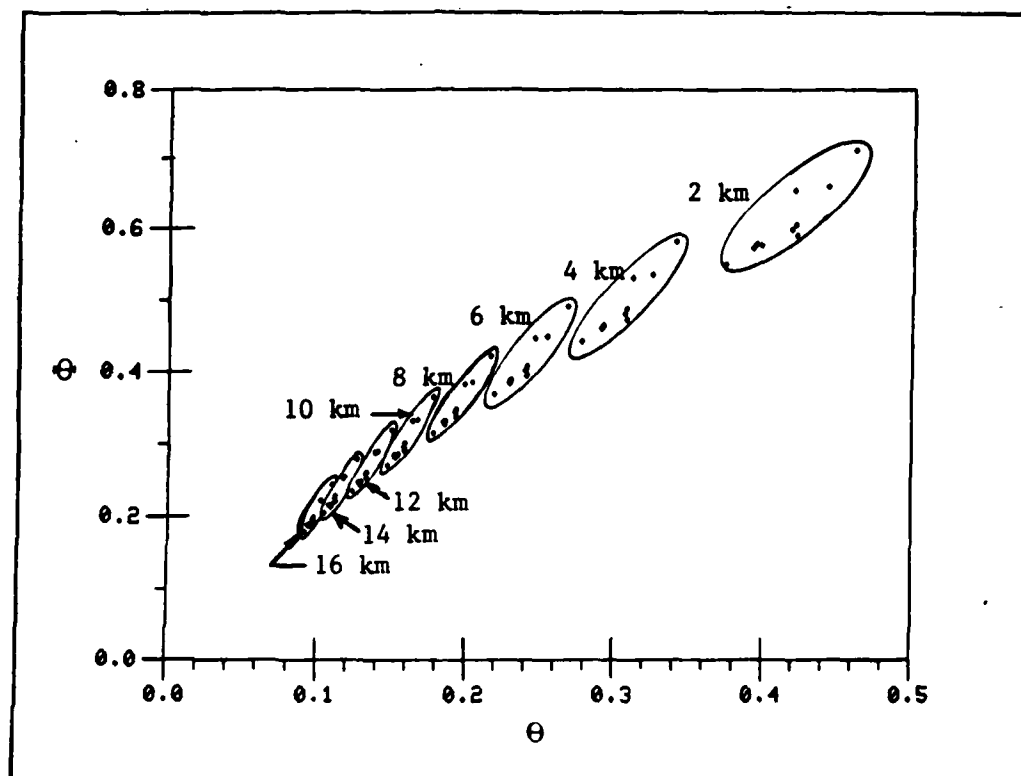


Figure 13. Range Distributions for ARI Sources Using Three Colors

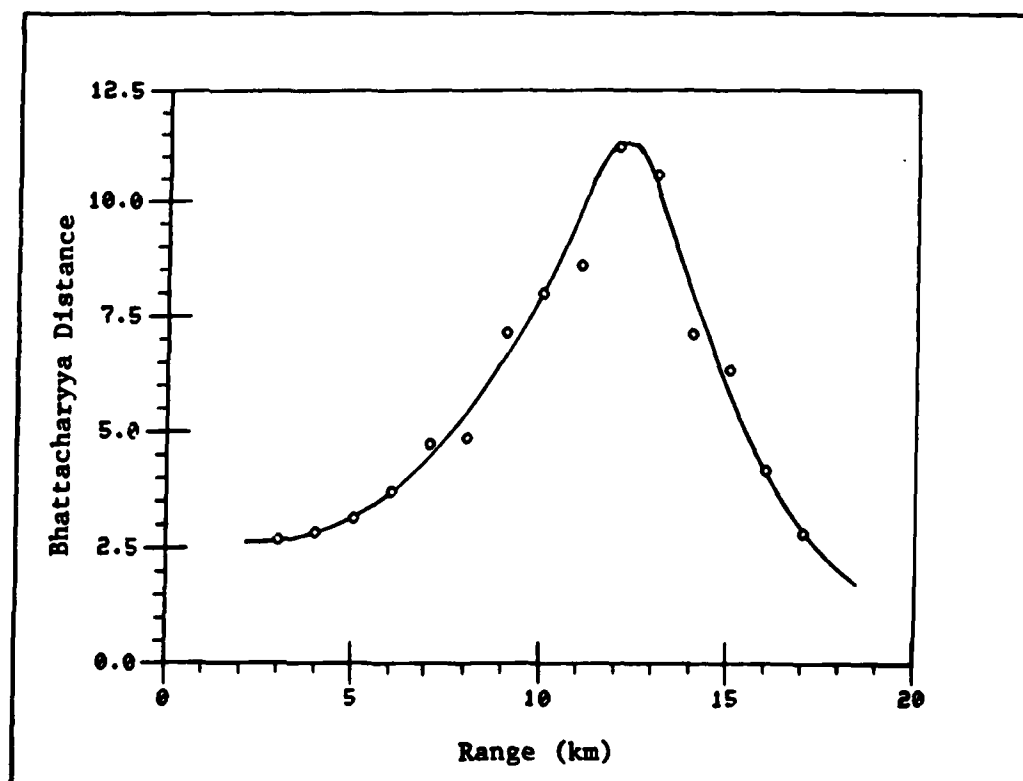


Figure 14. Bhattacharyya Separation for ARI Sources Using Three Colors

range until 13 km, and then drops rapidly. Even though the distributions appear to get closer together, Bhattacharyya distance is measured relative to the variance of the distributions which also decreases. The net effect is an increase in the Bhattacharyya distance until 13 km where the separation between the means becomes small compared to the variance.

Significant improvement is obtained in Bhattacharyya separation between distributions by using the third band. In the next chapter, the mean and covariance matrix of these distributions will be used to form the decision regions into which unclassified sources will be assigned. Before proceeding, the effect of background radiation on the Bhattacharyya separation will be investigated.

#### Background Fluctuations

The normalized distributions that represent range clusters in color space were formed assuming no background radiation contributions. Because sensors can be AC-coupled to remove the DC component of the noise signal, the only effect a background will have is to add fluctuations to the received source signals. The location of the means of the range clusters in color space will therefore remain the same, but the variances and covariances will increase. Because of this effect, the Bhattacharyya distances previously obtained represent the upper limit of a noise-free background. Bhattacharyya distances will decrease with the

addition of noise fluctuations.

To quantitatively account for noise, a covariance matrix representing the fluctuations of the received signals must be determined. Because the range covariance is statistically independent of the noise covariance, the total covariance matrix is the sum of the two independent covariance matrices (Ref 13:37).

The Environmental Research Institute of Michigan (ERIM) has published comprehensive and well documented background data in the mid-infrared region of the spectrum (Ref 14), and the measured data has been extensively analysed in an unpublished report (Ref 11). In Appendix C, an expression for the noise variance in the bands previously used is obtained based on this report. The value obtained for the noise variance in each  $25 \text{ cm}^{-1}$  band is

$$\sigma^2 = 3.75 \times 10^{-3} R^2 (\text{W/sr})^2 \quad (16)$$

where

$R$  = distance from source to sensor

Because the range clusters are formed in reduced color space, the variance in each band needs to be converted to a variance in terms of  $\theta$  and  $\phi$ . This is done through differentiation of the coordinate transforms and the details are shown in Appendix D. The result is an expression for the variance of  $\theta$  and  $\phi$  in terms of the variance obtained in Appendix C. To complete the covariance matrix, a value for

the correlation must be obtained. Relying on the measured data by ERIM, the correlation is estimated to be 0.7 (Ref 11). An accurate estimate of the correlation is not possible, but the effect on the results is minimal anyway. The diagonal elements of the covariance matrix (the variances) have the most significant effect. The background covariance matrix that was added to the range distribution covariance matrices is therefore:

$$C_n = \begin{bmatrix} (d\theta)^2 & (0.7)(d\theta)(d\phi) \\ (0.7)(d\theta)(d\phi) & (d\phi)^2 \end{bmatrix}$$

where  $d\theta$  and  $d\phi$  are defined in Appendix D by equations 36b and 37c.

The covariance matrix for noise fluctuations depends on range ( $d\theta$  and  $d\phi$ ) because the area of the background seen by the sensor depends on how far away the sensor is from the background. As the detected area increases, so does the magnitude of the fluctuations in the received signal. Also associated with the range is the attenuation of the fluctuations because of atmospheric absorption.

The covariance matrices of the range distributions were added to the covariance matrices of the noise fluctuations and the Bhattacharyya distances were recalculated. The effect of the noise covariance on the Bhattacharyya distances depends on the source intensity. In rectangular coordinates, the magnitude of the fluctuations is constant, but by using spherical coordinates to locate the distri-

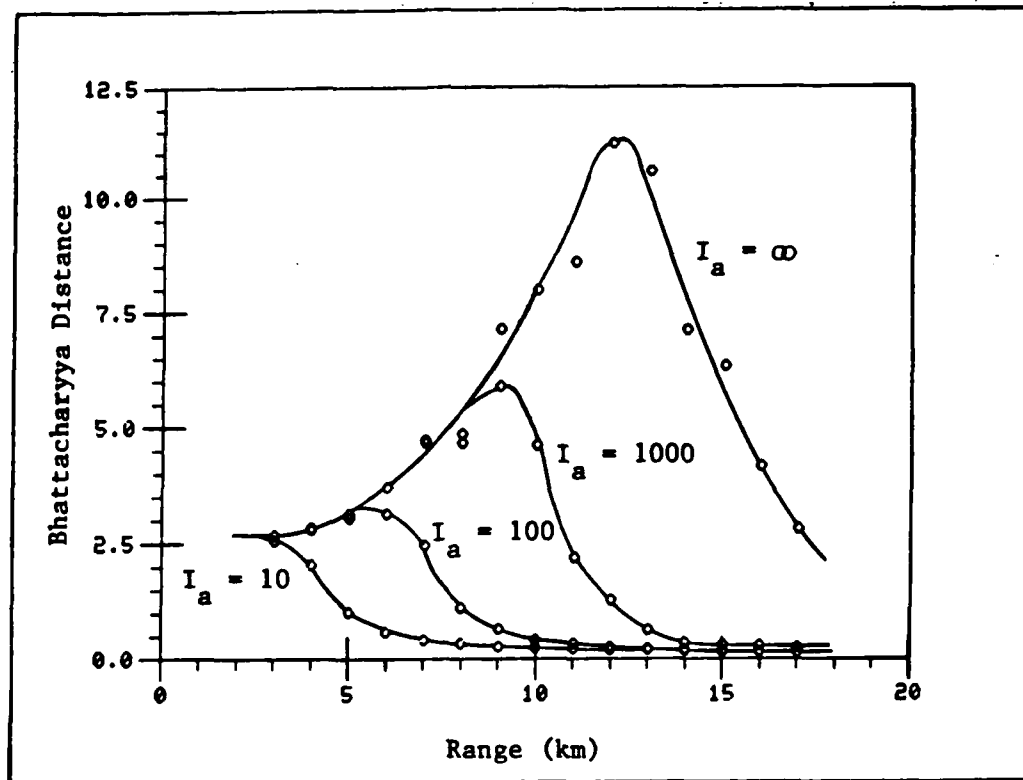


Figure 15. Bhattacharyya Separation for ARI Sources With Noise Added ( $I_a$  in W/sr at 2 km in band 2200-2225)

butions, the dependence on the source intensity is introduced. Weak sources relative to the background signal are affected more, so the separation between range distributions decreases more.

The results of the calculations are plotted in Figure 15. The plot labeled as infinite intensity is actually the original Bhattacharyya measures with no noise added (the result is the same). The intensity  $I_a$  is an apparent intensity at 2 km in the band 2200-2225  $\text{cm}^{-1}$ . The apparent intensity at 2 km is given by:

$$I_a = I_o \tau \quad (17)$$

where

$I_o$  = intensity at the source

$\tau$  = transmittance of the atmosphere

$I_a$  is called an apparent intensity because it does not include the inverse square variation with range.

As expected, the Bhattacharyya separation decreases as the intensity of the source becomes weaker. When the source intensity is much larger than the background variance, the Bhattacharyya distance is not affected. As the range increases, a point is reached where the Bhattacharyya separation falls off abruptly. This is the range at which the source signal would be hidden by the background and the range estimate obtained would be unreliable.

If the range increment between distributions is increased, the Bhattacharyya distance will also increase. The range increment that maintains a Bhattacharyya separation of 2.0 is plotted in Figure 16. For infinite intensity (no noise), range increments of less than 2 km will maintain Bhattacharyya separation of 2.0 until 18 km. For an apparent source intensity of 10 W/sr at 2 km, range distributions separated by 2 km maintain a Bhattacharyya separation of 2.0 only to 4 km. Beyond 5 km, a Bhattacharyya separation of 2.0 cannot be maintained regardless of the range increment. Because a Bhattacharyya separation of 2.0 represents little overlap between distributions, the



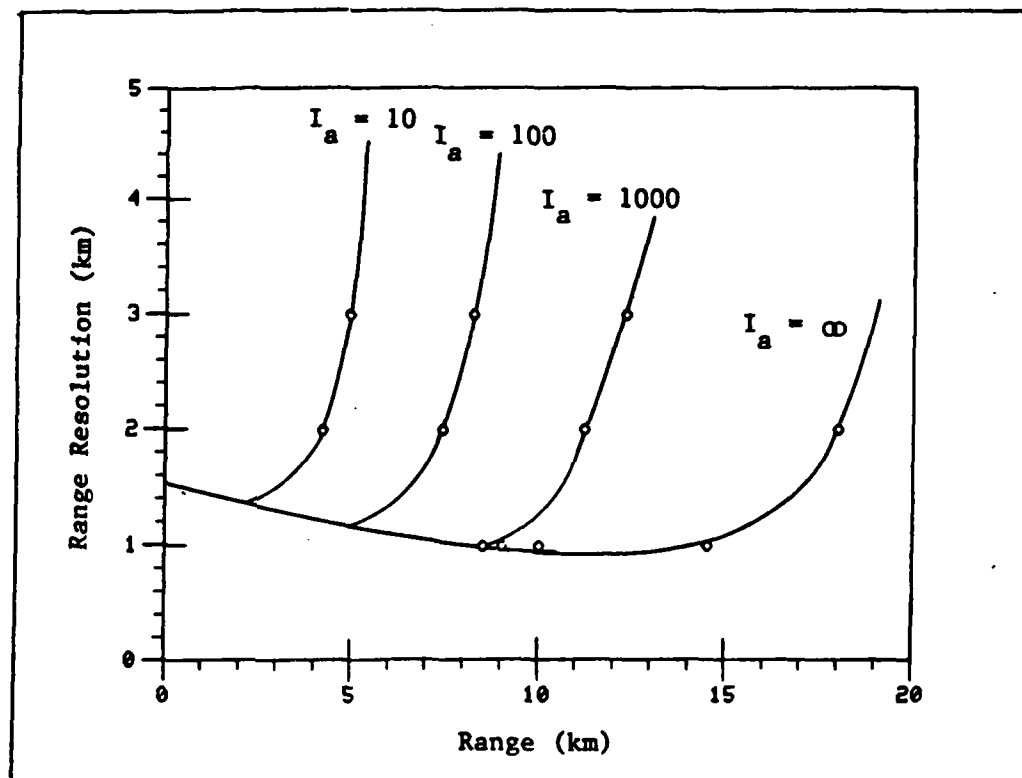


Figure 16. Range Resolution of ARI Sources With Noise Added

plot in Figure 16 can be considered to be an estimate of the range resolution that can be obtained for the given intensities.

## V. Ranging Algorithm

### Development

In the previous chapter, spectral bands were chosen so that the separation between range distributions in color space was maximized. The resulting normal distributions can be used to determine decision regions into which unknown sources will be classified.

All points were fitted to an Nth degree polynomial in  $\epsilon$  using a least squares method. The order of the polynomial was increased until the coefficient of determination exceeded 0.98. Only the distributions representing ranges between 2 and 18 km were used. Above 18 km, the extinction of the spectra becomes too large to permit reliable results. Below 2 km, the range distributions change rapidly and low order polynomials do not accurately predict the functions. All ranges below 2 km will therefore be assigned to the same decision region.

All data points listed in Appendix B were plotted in Figure 13. In Figure 17, only the means of the range distributions are plotted. A second order polynomial  $F(\epsilon)$  that can be used to predict the curve of the means is also plotted on the same graph. From the data obtained with the ARI files, the function  $F(\epsilon)$  was found to be:

$$F(\epsilon) = 0.0310 + (1.9339)\epsilon - (1.3125)\epsilon^2 \quad (18)$$

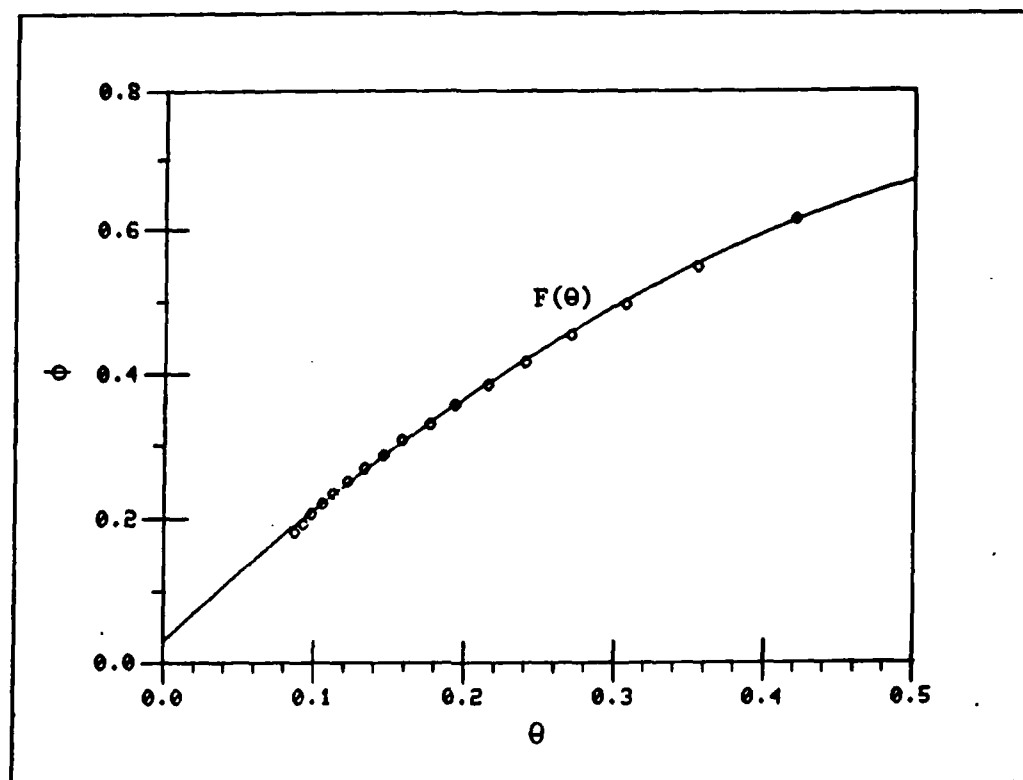


Figure 17. Mean of Each Range Distribution

Each point on this curve represents the location of the mean of a normalized distribution for a particular range.

By adding a third dimension to the same coordinate system, the range for each point of  $F(\theta)$  could be plotted on a separate axis. The result is a function in  $\theta$  and  $\phi$  that represents the range of each distribution. However,  $\phi$  is a dependent variable represented by  $F(\theta)$ , and the function would not be defined for all independent values of  $\theta$  and  $\phi$ . The range function actually depends on only one independent variable and can therefore be represented by a function  $R(\theta)$ . The range of each distribution as a function of  $\theta$

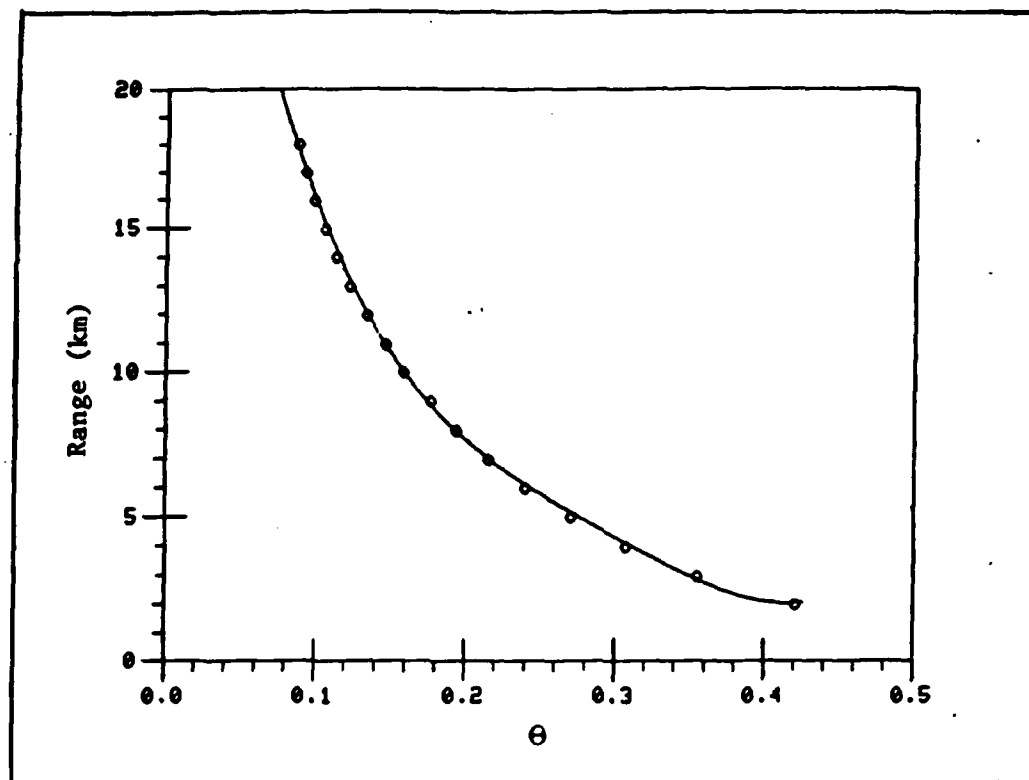


Figure 18. Range of Each Distribution

only is plotted in Figure 18. The fourth order polynomial  $R(\theta)$  that will predict range is also plotted, and is given by:

$$R(\theta) = 40.9698 - (395.7266)\theta + (1815.1719)\theta^2 - (4032.4529)\theta^3 + (3400.9910)\theta^4 \quad (19)$$

For  $R(\theta)$  to be valid though, the value of  $\theta$  must lie on the curve of the means.

When an unclassified source is plotted in reduced color space, it generally does not fall on the curve of the means. To calculate a range for the point using  $R(\theta)$ , the point

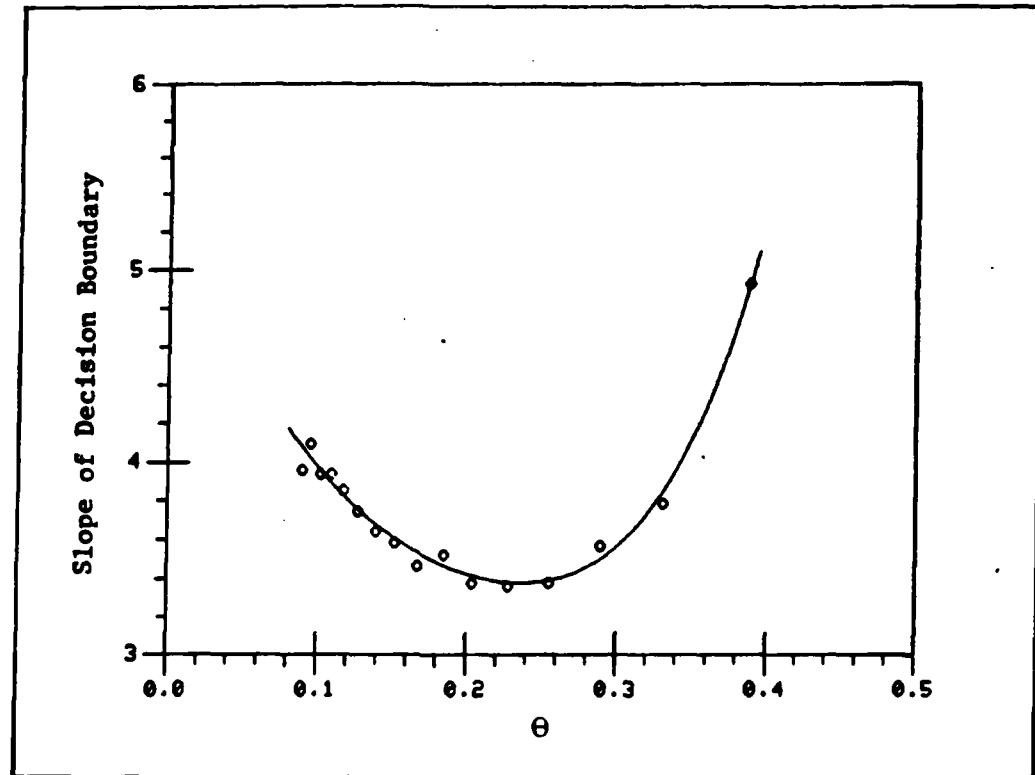


Figure 19. Slope of Decision Boundary Between Distributions

must first be projected onto  $F(\theta)$ . This projection should follow the decision boundaries that separate the distributions. If it is assumed that the covariance matrix for each distribution changes slowly, the decision boundaries for points near the curve of the means are linear. The slopes of these decision lines vary along  $F(\theta)$ .

A method to calculate the slope of the line separating two distributions whose covariance matrices are equal is given in Appendix A. Using this method, the slopes of linear decision boundaries between each distribution derived in Chapter IV was calculated. The results are plotted in

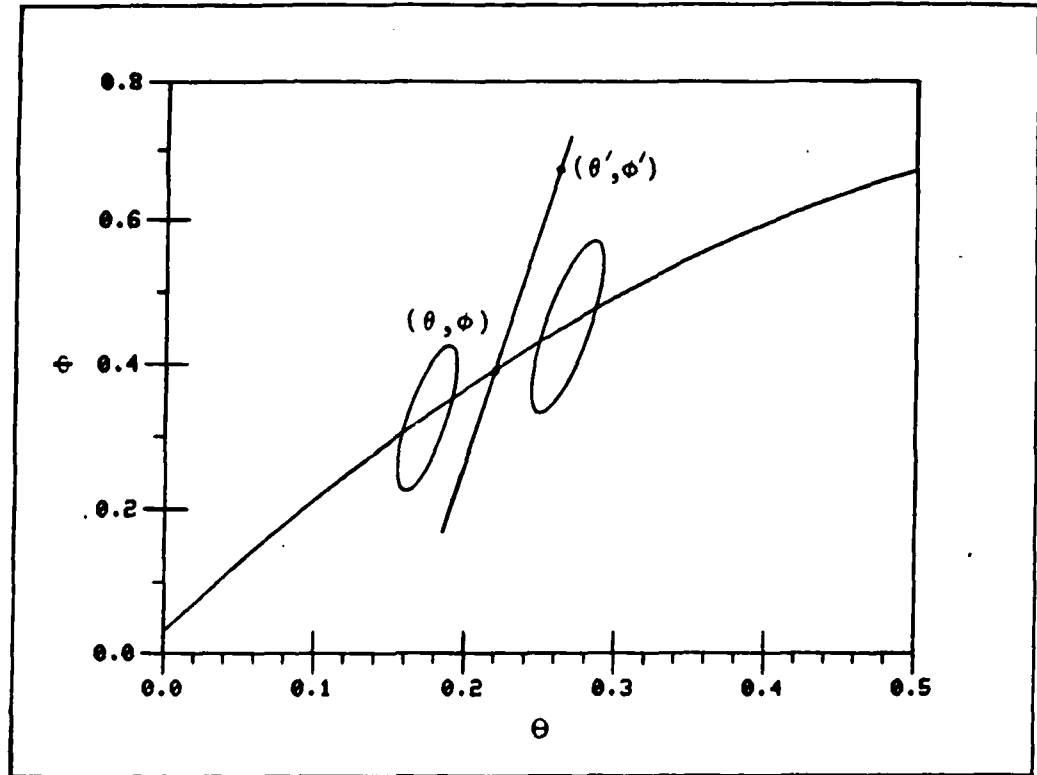


Figure 20. Projection of Unknown Source Along Decision Boundaries

Figure 19. For  $\theta$  values representing the means of range distributions between 2 and 18 km, the slope of the decision boundaries can be represented by the fourth order polynomial  $M(\theta)$  also plotted in Figure 19 and given by:

$$M(\theta) = 5.6837 - (27.7977)\theta + (142.5650)\theta^2 - (412.0620)\theta^3 + (557.0090)\theta^4 \quad (20)$$

If the values of  $\theta'$  and  $\phi'$  in Figure 20 represent an unclassified source in reduced color space, the slope of the line between the points  $(\theta', \phi')$  and  $(\theta, \phi)$  is given by:

$$m = (\phi' - \phi) / (\theta' - \theta) \quad (21)$$

where

$(\theta, \phi)$  = unknown projection of  $(\theta', \phi')$  onto  $F(\theta)$

Because the point  $(\theta, \phi)$  lies on  $F(\theta)$ , the value of  $\phi$  can be represented by  $F(\theta)$ . In addition, the value of  $m$  can be represented by  $M(\theta)$ . The result is a fifth order polynomial in  $\theta$  given by

$$M(\theta) = \frac{\phi' - F(\theta)}{\theta' - \theta} \quad (22)$$

Solving this equation for  $\theta$  and substituting in values obtained from the ARI files,

$$0 = C_0 + C_1\theta + C_2\theta^2 + C_3\theta^3 + C_4\theta^4 + C_5\theta^5 \quad (23)$$

where

$$C_0 = (-5.6837)\theta' - 0.0310 + \phi'$$

$$C_1 = (27.7977)\theta' - 1.9339 + 5.6837$$

$$C_2 = (-142.5650)\theta' + 1.3125 - 27.7977$$

$$C_3 = (412.0620)\theta' + 142.5650$$

$$C_4 = (-557.0090)\theta' - 412.0620$$

$$C_5 = 557.0090$$

The solution to this equation is a value for  $\theta$  that is used in the range function  $R(\theta)$ . Because the equation is a fifth order polynomial, there are five possible roots. However, there is only one real root for values of  $\theta$  that represent ranges between 2 and 18 km. The polynomial was solved by

calling a subroutine in an IMSL library (Ref 15).

Using this method, any value of  $\theta'$  and  $\phi'$  can be projected onto the curve of the means and a range calculated using the function  $R(\theta)$ . Because the decision boundaries are not actually linear, projection accuracy decreases as the distance from the curve of the means increases.

### Testing

Although spectral regions are chosen that minimize the effect of LOWTRAN model variations, some inaccuracy is expected when atmospheric conditions are different from the U.S. standard atmosphere that was used in developing the distributions. Using LOWTRAN model 6 (U.S. standard), spectra simulating unknown ranges were created from the ARI files. The predicted ranges are shown in Table III for several ranges. The range for all sources fell within 0.8 km of the LOWTRAN simulated range. This implies that the analysis is self-consistent since the 1962 U.S. Standard atmospheric model was the only one used to generate the distributions.

The ARI files were then multiplied by LOWTRAN transmittance from model 2 (mid latitude summer) and model 3 (mid latitude winter), and the range estimates for these files are also listed in Table III. Using model 2, the range estimates were consistently low; for model 3, the estimates were consistently high. These are considered systematic errors and could be accounted for relatively



Table III  
Computed Ranges For ARI Files

(a) LOWTRAN Model 6 (U.S. Standard)

File	2 km	5 km	8 km	11 km	14 km	17 km
003	(2)	4.8	7.8	10.8	14.2	16.2
015	(2)	4.6	7.7	11.0	14.4	16.6
017	(2)	4.6	7.6	10.9	14.4	16.6
019	2.1	5.4	8.2	11.3	14.8	16.9
035	(2)	5.0	7.9	11.0	14.5	16.6
050	2.1	5.3	8.1	11.0	14.3	16.4
052	2.1	5.3	8.1	11.0	14.3	16.4
053	2.0	5.4	8.3	11.3	14.7	16.7
054	2.4	5.6	8.4	11.4	14.6	16.7

(2) = less than 2 km

(b) LOWTRAN Model 2 (Mid Latitude Summer)

File	2 km	5 km	8 km	11 km	14 km	17 km
003	(2)	4.3	6.9	9.7	12.4	14.1
015	(2)	4.5	7.1	9.8	12.7	14.6
017	(2)	4.5	7.0	9.8	12.6	14.5
019	2.0	4.8	7.4	10.2	13.0	14.9
035	(2)	4.4	7.0	9.9	12.7	14.5
050	2.1	4.8	7.3	9.9	12.6	14.5
052	2.1	4.8	7.2	9.9	12.6	14.4
053	(2)	4.8	7.4	10.2	12.9	14.6
054	2.2	5.1	7.5	10.3	12.9	14.8

(c) LOWTRAN Model 3 (Mid Latitude Winter)

File	2 km	5 km	8 km	11 km	14 km	17 km
003	(2)	5.5	8.8	12.6	16.1	18.0
015	2.1	5.6	8.9	12.8	16.3	18.4
017	2.1	5.6	8.9	12.7	16.3	18.4
019	2.3	5.9	9.2	13.1	16.6	18.7
035	2.0	5.6	8.9	12.9	16.4	18.4
050	2.3	5.9	9.1	12.8	16.2	18.2
052	2.3	5.9	9.0	12.7	16.1	18.1
053	2.2	6.0	9.3	13.1	16.5	18.4
054	2.7	6.2	9.4	13.1	16.5	18.5

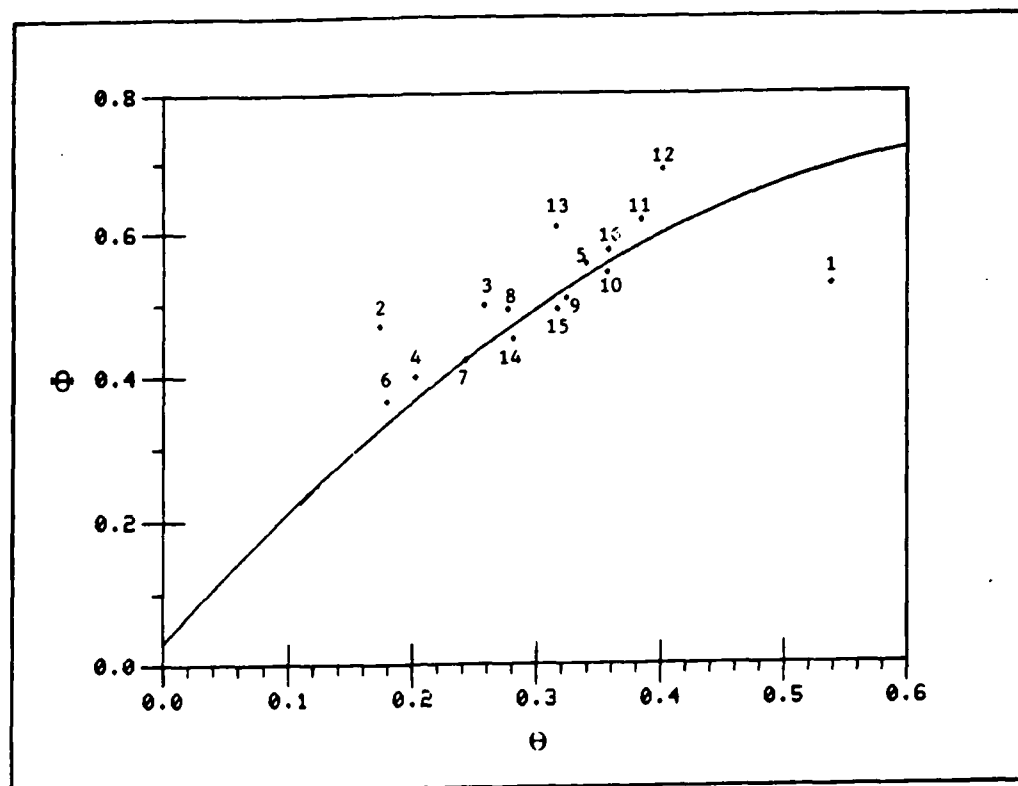


Figure 21. Location of AFG Files in Color Space

easily by inputting an atmospheric factor prior to using the algorithm. In any case, the range estimates are still good, especially at close ranges.

The sixteen spectra from the AFG library representing various infrared sources at unknown ranges were then tested using the algorithm. The reduced color space plot of all the sources is shown in Figure 21 in relation to the mean curve  $F(\Theta)$ . Except for four files (#1, #2, #12, and #13), all points fall reasonably close to  $F(\Theta)$ . Had they not fallen near the curve, the validity of the algorithm would be questionable. This would imply that the sources are

Table IV  
Range Comparison For AFG Files

File Number	Actual Range (km)	Calc. Range (km)	Error (km)
01	3.5	(2)	-1.5
02	3.5	14.7	11.2
03	3.9	6.5	2.6
04	4.7	8.4	3.7
05	4.4	3.4	-1.0
06	4.7	9.8	5.1
07	2.8	6.1	3.3
08	4.4	5.4	1.0
09	3.2	3.6	0.4
10	3.2	2.8	-0.4
11	3.3	2.5	-0.8
12	2.9	2.4	-0.5
13	2.9	5.1	2.2
14	3.1	4.7	1.6
15	2.6	3.7	1.1
16	2.7	3.0	0.3

substantially different from the types that generated the original distributions, and new distributions should be formed to include the new sources. By doing this, the coefficients of the ranging algorithm would change. In some cases, it may be necessary to change the band selection and recalculate the ranging algorithm entirely. The best way to determine the effectiveness of the algorithm is to test it on as many sources as possible.

The calculated range of each AFG file is compared to the actual range in Table IV. Ten of the sixteen files have actual ranges that are within 2 km of the calculated ranges.

Twelve are within 2.6 km. Only four files resulted in errors greater than 3 km. Of these four files, one is hot metal (#02), one is a flare stack (#04), one is a blast furnace (#06), and one is a coke oven (#07). There is no consistency to the source type. Two of the four spectra were recorded at sites in Michigan, and two were recorded in Indiana. Other sources in these areas provided good range estimates.

It has been shown with the ARI files that atmospheric conditions can cause systematic errors. Because the AFG files were recorded at different locations and on different days, it is impossible to determine if the errors are indeed systematic. Most of the files have range estimates that are longer than the actual ranges, but the difference due to atmospheric variations is questionable.

It is suspected that errors from subtracting the background spectra from the composite spectra contribute to the range error. It has been noted (Ref 5) that errors of 25% are possible, and variations of that magnitude certainly would affect the results.

In the reduced color space plot of the spectra (Figure 21), three of the four points fall fairly close to the curve of the means. Only one point (#02) appears to be far from the curve. However, the point for file #12 also plotted far from the curve and resulted in an accurate prediction. None of these reasons can justify why the four files resulted in

inaccurate predictions.

The cause of the error can be determined through a careful analysis of the source spectra. There is a sharp spike on all source spectra near  $2200\text{ cm}^{-1}$ . This is caused by the absorption from  $\text{N}_2\text{O}$  at  $2224\text{ cm}^{-1}$  (Ref 16:40). Because the peak that remains is almost completely in band 2, the ratio of band 3 to band 2 is small. The ranging algorithm interprets this as a source at a longer range than it actually is.

This  $\text{N}_2\text{O}$  spike did not occur when setting up the distributions using ARI files and LOWTRAN. The  $20\text{ cm}^{-1}$  wavenumber resolution of LOWTRAN averaged the spike out to a smooth spectral curve. The distributions were formed by comparing bands in which there was no  $\text{N}_2\text{O}$  spike.

There are two possible solutions to this problem. One is to use a higher resolution atmospheric model and reform the distributions so the ranging algorithm can be corrected. The other possible solution is to average the AFG spectrum over a  $20\text{ cm}^{-1}$  wavenumber bandwidth and then test the algorithm on the averaged spectrum. Either of these methods should improve the accuracy of the estimates.

## VI. Conclusion

### Summary

The atmosphere is almost always considered a hinderance to the detection of electromagnetic radiation. However, through a careful analysis of the effect of the atmospheric absorption on an infrared signature, it is possible to estimate the range of an emitter. Although the accuracy of the method is limited, the entire process is passive. Any received signal at the proper frequency ( $2175\text{--}2250\text{ cm}^{-1}$ ) will result in an instantaneous estimate of the source's range.

Spectral discrimination methods were presented that allowed the analysis to be independent of source intensity. Distributions of spectral representations in color space were formed by comparing several frequency bands within a received signal. Bhattacharyya distances were calculated to compare the separation between each range distribution, and the bands were adjusted to optimize the separation.

Using two frequency bands at  $2175\text{--}2200\text{ cm}^{-1}$  and  $2200\text{--}2225\text{ cm}^{-1}$ , blackbody range distributions were separated by a Bhattacharyya distance of 2.0 to a range of 10 km. When actual sources were tested using these bands, the Bhattacharyya distance did not reach 2.0 for any range. The bands were adjusted to  $2200\text{--}2225\text{ cm}^{-1}$  and  $2225\text{--}2250\text{ cm}^{-1}$ , and the Bhattacharyya distance reached 2.0, but only through 5 km.

Three colors had to be used to improve this separation.

The optimum spectral region for comparing the IR signatures with three colors was between 2175 and 2250  $\text{cm}^{-1}$ . Division of this region into three 25  $\text{cm}^{-1}$  wide bands provided Bhattacharyya distances of 2.0 between range distributions separated by 2 km out to ranges of 18 km. The mean and covariance matrix of each distribution was used to develop a ranging algorithm. By using the algorithm on the sources that generated the distributions, range estimates within 0.8 km were obtained. This verified the validity of the method. If a source of unknown range is of the same type as the ones that generated the ranging algorithm, an accurate estimate of range should be obtained.

The atmospheric model used to simulate range for the sources was then varied. As expected, the range errors increased, but the predictions remained within 2.0 km of the actual range for 87% of the files. The algorithm is relatively independent of atmospheric variations, but a more accurate prediction can be obtained if an atmospheric factor is applied to the algorithm.

In developing the analysis, it was found that cool gas sources that emitted little radiation beyond the atmospheric absorption band could not provide an accurate range estimate. The algorithm depends on sources having relatively constant intensities between 2175-2250  $\text{cm}^{-1}$  so that all intensity differences within the comparison bands can be

interpreted as range effects. Radiation intensity of cool gas sources begins to decrease rapidly below  $2200\text{ cm}^{-1}$ , and the algorithm incorrectly interprets this as a range effect.

Only a limited number of source spectra were available to test the ranging algorithm. Of the sixteen spectra, twelve provided range estimates within 2.6 km of the measured ranges. Ten were within 1.6 km of the specified ranges. The errors were mainly caused by a radiation spike at  $2224\text{ cm}^{-1}$  from  $\text{N}_2\text{O}$ . This spike causes one of the band intensities to be excessively large, and the ranging algorithm assigns a much longer range to the spectrum than it should. Because of the resolution of LOWTRAN, the spike was smoothed out when the algorithm was developed, so it should be possible to correct the error by using an atmospheric model with a higher resolution.

Background noise severely degraded the separation that could be obtained from range distributions, and the amount of degradation depends on the source intensity. For intense sources, range resolution of 2 km is theoretically maintained out to ranges of 18 km, but this resolution rapidly decreased as the source intensity became weaker.

#### Recommendations

Many restrictions had to be placed on the atmospheric conditions that generated the distributions. By relaxing some of these restrictions, a better idea of the sensitivity to various climates and weather conditions could be



obtained. The path between source and sensor was also limited to sea level altitudes. Variations caused by changing the path profiles could also be investigated.

Several sources did not result in an accurate range prediction. The  $N_2O$  spike at  $2224\text{ cm}^{-1}$  causes a high intensity in one of the bands and the ranging algorithm interprets this as a source at a long range. Cool gas sources also do not result in accurate range estimates. It may be possible to sort these types of source spectra into different classes and use different ranging algorithms to estimate the range of sources in these classes.

Unfortunately, all of the AFG files used to test the algorithm were not hot gas sources, and the ranges of these sources was limited. More source spectra should be obtained to further test the ranging algorithm. Sources representing aircraft and missiles at ranges up to 20 km would be ideal. The algorithm determined in this study may work very well on hot gas sources, but this could not be verified using the limited sources available.

## Appendix A

### Linear Decision Functions

When two Gaussian distributions are located in a two dimensional coordinate system, the decision boundary separating the two distributions is quadratic (Ref 8:53). In Figure 8, a quadratic decision boundary was constructed by plotting the intersection of contours of equal probability of the distribution functions for both distributions. If the distributions have equal covariance matrices, the decision boundary becomes linear. The slope of the line separating two distributions of equal covariance is derived in this appendix.

To find points that define the intersection of isoprobability contours, the probability functions of the distributions are set equal. The solution to the resulting equation is the set of points that represent the same probability of falling in either distribution. The probability function for a Gaussian distribution is given by (Ref 10:35):

$$p(\bar{X}) = (2\pi)^{-d/2} |\underline{C}|^{-1/2} \exp \left[ \frac{1}{2} (\bar{X} - \bar{M})^T \underline{C}^{-1} (\bar{X} - \bar{M}) \right] \quad (10)$$

where

- d = dimension of  $\bar{X}$
- $\bar{X} = (x_1, x_2, \dots, x_d)$
- $\bar{M}$  = mean of the distribution
- $\underline{C}$  = covariance matrix of the distribution

$|\underline{C}|$  = determinant of  $\underline{C}$

$\underline{C}^{-1}$  = inverse of  $\underline{C}$

In two dimensions, the covariance matrix is given by:

$$\underline{C} = \begin{bmatrix} \sigma_1^2 & r\sigma_1\sigma_2 \\ r\sigma_1\sigma_2 & \sigma_2^2 \end{bmatrix} \quad (24)$$

where

$\sigma$  = standard deviation

Inversion of this matrix yields

$$\underline{C}^{-1} = \frac{1}{1-r^2} \begin{bmatrix} \frac{1}{\sigma_1^2} & \frac{-r}{\sigma_1\sigma_2} \\ \frac{-r}{\sigma_1\sigma_2} & \frac{1}{\sigma_2^2} \end{bmatrix} \quad (25)$$

When covariance matrices are equal, equating the probability functions is equivalent to equating only the exponents of the probability functions. The result is

$$(\bar{X}_1 - \bar{M}_1)^T \underline{C}^{-1} (\bar{X}_1 - \bar{M}_1) = (\bar{X}_2 - \bar{M}_2)^T \underline{C}^{-1} (\bar{X}_2 - \bar{M}_2) \quad (26)$$

Letting  $\bar{M}_i = (x_i, y_i)$ , this equation can be reduced to

$$y = \frac{(x_2 - x_1)\sigma_2^2 - (y_2 - y_1)r\sigma_1\sigma_2}{(x_2 - x_1)r\sigma_1\sigma_2 - (y_2 - y_1)\sigma_1^2} (x) + \text{Constant} \quad (27)$$

Obviously, this is the equation of a line whose slope is given by the coefficient of  $x$ . Knowing the location of the means of two distributions and assuming equal covariance,

the slope of the line that defines the decision boundary between the two distributions can be calculated.

## Appendix B

### Computed Data for ARI Files

In Figure 14, the locations of the points representing the color space location of all the ARI files at several LOWTRAN ranges were plotted. The tabulated data in this appendix is the computed values that generated that graph.

All values were computed using the following three bands to compare the relative intensities of a spectrum:

band 1: 2200 - 2225  $\text{cm}^{-1}$

band 2: 2225 - 2250  $\text{cm}^{-1}$

band 3: 2175 - 2200  $\text{cm}^{-1}$

These bands are not in increasing order because band 1 and band 2 are the same bands that were used with two colors. It should be noted also that the sequence of bands affects the values that will be computed for  $\theta$  and  $\phi$ . When converting to spherical coordinates from rectangular coordinates, the values of x, y, and z are not interchangeable.

The first column of the tables is self-explanatory. The column labeled LOWT is the LOWTRAN atmospheric model that was used. "M6" stands for model 6, and "R\*\*" is the range in km. The next three columns labeled Band 1, 2, and 3 are the actual integrated intensities of each band in units of source intensity (W/sr). The magnitudes are different because some sources are brighter than others. The columns labeled Angle 1 and Angle 2 are the values of  $\theta$  and  $\phi$  respectively that are used in the distributions. Even though the

intensity of the sources varies by three orders of magnitude, the values of  $\theta$  and  $\phi$  are fairly close. The mean and standard deviation of each range distribution are also given.

Table V  
ARI Computed Data

TYPE	LOWT	BAND 1	BAND 2	BAND 3	ANGLE 1	ANGLE 2
BB @ 2000.						
ARILIB.003	M6R2	2.78E+01	1.25E+01	4.50E+01	0.4210	0.5957
ARILIB.015	M6R2	7.07E+00	3.51E+00	9.03E+00	0.4607	0.7181
ARILIB.017	M6R2	5.85E+01	4.40E+01	1.54E+02	0.4206	0.6112
ARILIB.019	M6R2	8.40E+01	3.73E+01	1.33E+02	0.4183	0.6038
ARILIB.035	M6R2	5.70E+00	2.39E+00	9.39E+00	0.3973	0.5820
ARILIB.050	M6R2	2.48E+01	1.17E+00	3.49E+00	0.4419	0.6656
ARILIB.052	M6R2	9.15E+01	3.80E+01	1.50E+02	0.3923	0.5834
ARILIB.053	M6R2	1.35E+01	3.23E+01	1.30E+02	0.3923	0.5771
ARILIB.054	M6R2	5.30E+03	6.03E+00	1.91E+01	0.4193	0.6552
			2.07E+03	9.17E+03	0.3734	0.5551
				AVERAGE:	0.4139	0.6151
				STD DEV:	0.0256	0.0503
BB @ 2000.						
ARILIB.003	M6R4	1.64E+01	5.20E+00	3.31E+01	0.3076	0.4791
ARILIB.015	M6R4	4.15E+00	1.47E+01	6.61E+00	0.3402	0.5875
ARILIB.017	M6R4	5.80E+01	1.84E+01	1.13E+02	0.3076	0.4934
ARILIB.019	M6R4	4.94E+03	1.56E+01	9.79E+01	0.3058	0.4869
ARILIB.035	M6R4	3.36E+03	1.01E+03	6.51E+03	0.2916	0.4695
ARILIB.050	M6R4	1.46E+00	4.88E-01	2.56E+00	0.3238	0.5408
ARILIB.052	M6R4	5.38E+01	1.61E+01	1.10E+02	0.2913	0.4709
ARILIB.053	M6R4	4.60E+01	1.37E+01	9.56E+01	0.2899	0.4655
ARILIB.054	M6R4	7.95E+00	2.55E+00	1.40E+01	0.3107	0.5374
			8.87E+02	6.76E+03	0.2769	0.4475
				AVERAGE:	0.3045	0.4979
				STD DEV:	0.0183	0.0435
BB @ 2000.						
ARILIB.003	M6R6	1.04E+01	2.59E+00	2.58E+01	0.2401	0.4005
ARILIB.015	M6R6	2.67E+00	7.32E-01	5.12E+00	0.2672	0.4963
ARILIB.017	M6R6	3.75E+01	9.18E+00	8.80E+01	0.2402	0.4134
ARILIB.019	M6R6	3.20E+01	7.75E+00	7.62E+03	0.2388	0.4077
ARILIB.035	M6R6	2.17E+03	5.05E+02	5.38E+03	0.2284	0.3929
ARILIB.050	M6R6	9.40E-01	2.43E-01	1.99E+00	0.2531	0.4549
ARILIB.052	M6R6	3.48E+01	8.13E+00	8.60E+01	0.2296	0.3941
ARILIB.053	M6R6	2.97E+01	6.92E+00	7.44E+01	0.2284	0.3893
ARILIB.054	M6R6	5.13E+00	1.28E+00	1.09E+01	0.2451	0.4527
			4.49E+02	5.27E+03	0.2188	0.3741
				AVERAGE:	0.2390	0.4176
				STD DEV:	0.0140	0.0381

TYPE	LOWT	BAND 1	BAND 2	BAND 3	ANGLE 1	ANGLE 2
BB @ 2000.						
ARILIB:003	M6R8	7.21E+00	1.41E+00	2.06E+01	0.1927	0.3421
ARILIB:015	M6R8	1.82E+00	3.97E-01	4.09E+00	0.2154	0.4270
ARILIB:017	M6R8	2.55E+01	4.98E+00	7.04E+01	0.1929	0.3537
ARILIB:019	M6R8	2.18E+03	4.23E+00	6.10E+01	0.1917	0.3488
ARILIB:035	M6R8	1.48E+03	2.75E+02	4.31E+03	0.1839	0.3359
ARILIB:035	M6R8	6.39E-01	1.32E-01	1.59E+00	0.2033	0.3405
ARILIB:050	M6R8	2.37E+01	4.45E+00	6.88E+01	0.1856	0.3369
ARILIB:052	M6R8	2.02E+01	3.78E+00	5.96E+01	0.1847	0.3327
ARILIB:053	M6R8	3.49E+00	7.01E-01	8.69E+00	0.1983	0.3888
ARILIB:054	M6R8	1.37E+03	2.46E+02	4.22E+03	0.1773	0.3194
				AVERAGE:	0.1926	0.3576
				STD DEV:	0.0110	0.0336
BB @ 2000.						
ARILIB:003	M6R10	5.06E+00	8.05E-01	1.68E+01	0.1579	0.2951
ARILIB:015	M6R10	1.77E+00	2.27E-01	3.32E+00	0.1771	0.3703
ARILIB:017	M6R10	1.53E+01	2.85E+00	5.74E+01	0.1581	0.3055
ARILIB:019	M6R10	1.04E+03	2.42E+02	4.98E+03	0.1571	0.3011
ARILIB:035	M6R10	4.48E-01	1.58E-02	3.52E+00	0.1510	0.2899
ARILIB:050	M6R10	1.66E+01	7.53E+00	1.62E+01	0.1667	0.3380
ARILIB:052	M6R10	1.42E+01	2.56E+00	5.67E+01	0.1530	0.2907
ARILIB:053	M6R10	2.44E+00	2.18E+00	4.87E+01	0.1523	0.2869
ARILIB:054	M6R10	9.64E+02	4.03E-01	7.07E+00	0.1636	0.3366
				AVERAGE:	0.1583	0.3089
				STD DEV:	0.0089	0.0297
BB @ 2000.						
ARILIB:003	M6R12	3.62E+00	4.84E-01	1.39E+01	0.1327	0.2569
ARILIB:015	M6R12	9.08E-01	1.36E-01	2.74E+00	0.1493	0.3237
ARILIB:017	M6R12	1.09E+01	1.71E+00	4.74E+01	0.1329	0.2663
ARILIB:035	M6R12	7.44E+02	1.45E+00	4.11E+01	0.1320	0.2624
ARILIB:050	M6R12	3.20E-01	9.51E-02	2.91E+03	0.1270	0.2525
ARILIB:052	M6R12	1.19E+01	1.54E+00	1.06E+00	0.1402	0.2951
ARILIB:053	M6R12	1.02E+01	1.31E+00	4.64E+01	0.1291	0.2531
ARILIB:054	M6R12	1.75E+00	2.43E-01	5.83E+01	0.1285	0.2497
				AVERAGE:	0.1236	0.2396
				STD DEV:	0.1333	0.2693
					0.0075	0.0263



TYPE	LOWT	BAND 1	BAND 2	BAND 3	ANGLE 1	ANGLE 2
BB @ 2000.						
ARILIB.003	M6R14	2.64E+00	2.96E-01	1.16E+01	0.1117	0.2247
ARILIB.015	M6R14	6.59E-01	8.35E-02	2.28E+00	0.1261	0.2839
ARILIB.017	M6R14	9.32E+00	1.05E+00	3.42E+01	0.1119	0.2331
ARILIB.019	M6R14	7.96E+02	8.88E-01	3.42E+01	0.1112	0.2297
ARILIB.035	M6R14	5.42E+01	5.83E+01	2.43E+03	0.1072	0.2210
ARILIB.050	M6R14	2.33E-01	2.76E-02	8.86E-01	0.1181	0.2587
ARILIB.052	M6R14	8.65E+00	9.49E-01	3.87E+01	0.1053	0.2214
ARILIB.053	M6R14	7.39E+00	8.07E-01	3.35E+01	0.1087	0.2184
ARILIB.054	M6R14	1.27E+00	1.49E-01	4.85E+00	0.1170	0.2575
	M6R14	5.03E+02	5.29E+01	2.38E+03	0.1048	0.2094
				AVERAGE:	0.1126	0.2358
				STD DEV:	0.0063	0.0233
BB @ 2000.						
ARILIB.003	M6R16	1.95E+00	1.85E-01	9.79E+00	0.0970	0.1970
ARILIB.015	M6R16	6.88E+00	6.35E-01	1.92E+01	0.1098	0.2495
ARILIB.017	M6R16	5.87E+00	6.71E-01	3.33E+01	0.0972	0.2045
ARILIB.019	M6R16	4.00E+02	5.69E-01	2.89E+03	0.0965	0.2015
ARILIB.035	M6R16	1.72E-01	3.74E+01	7.47E-01	0.0931	0.1938
ARILIB.050	M6R16	6.39E+00	1.77E-02	2.26E+01	0.1026	0.2272
ARILIB.052	M6R16	5.46E+00	6.10E-01	3.83E+01	0.0952	0.1941
ARILIB.053	M6R16	9.35E-01	5.19E-01	4.09E+00	0.0947	0.1914
ARILIB.054	M6R16	3.71E+02	5.58E-02	2.01E+03	0.1020	0.2261
				AVERAGE:	0.0980	0.2069
				STD DEV:	0.0054	0.0207
BB @ 2000.						
ARILIB.003	M6R18	1.45E+00	1.25E-01	8.31E+00	0.0865	0.1731
ARILIB.015	M6R18	3.60E-01	3.54E-02	1.62E+00	0.0981	0.2197
ARILIB.017	M6R18	5.12E+00	4.44E-01	2.82E+01	0.0866	0.1798
ARILIB.019	M6R18	2.98E+02	3.77E-01	2.45E+03	0.0860	0.1771
ARILIB.035	M6R18	1.28E-01	2.48E+01	1.74E+03	0.0831	0.1703
ARILIB.050	M6R18	4.75E+00	1.17E-02	6.32E-01	0.0915	0.1999
ARILIB.052	M6R18	4.06E+00	4.05E-01	2.77E+01	0.0850	0.1705
ARILIB.053	M6R18	6.94E-01	3.44E-01	2.40E+01	0.0846	0.1682
ARILIB.054	M6R18	2.76E+02	6.26E-02	3.46E+00	0.0912	0.1990
				1.70E+03	0.0816	0.1612
				AVERAGE:	0.0874	0.1819
				STD DEV:	0.0049	0.0183

Appendix C  
Noise Variance

By A-C coupling an IR detector's output, the average signal from a background becomes zero. The fluctuations from the background are still present though, and can be represented by a covariance matrix. The magnitude of the background fluctuations has been analyzed by Sanderson (Ref 11), and a brief summary is presented in this appendix to show how the actual value to use in the covariance matrix was obtained.

If  $F(\bar{x})$  represents the random distribution function that defines the fluctuations in the background intensity in a two dimensional scene, the auto-correlation function  $A(\bar{p})$  is given by

$$A(\bar{p}) = \int F(\bar{x}) F(\bar{x} + \bar{p}) d\bar{x} \quad (28)$$

The Fourier transform of the auto-correlation function is called the power spectrum and is denoted by:

$$W(\bar{k}) = \int A(\bar{p}) \exp(-2\pi i \bar{k} \cdot \bar{p}) d\bar{p} \quad (29)$$

A one-dimensional power spectrum is usually called the Wiener spectrum (Ref 3:XVII,9).

The variance of a noise signal can be obtained by integrating the power spectrum (Ref 11):

$$\sigma^2 = \int W(\bar{k}) d\bar{k} \quad (30)$$

Through an analysis of background spectra obtained from Environmental Research Institute of Michigan (ERIM), it is found that the power spectrum of most backgrounds varies as (Ref 11):

$$W(\bar{k}) = B/\bar{k} \quad (31)$$

where B is a constant that depends on the environmental conditions.

The integral of this function is divergent, which implies that power spectra by themselves cannot give an indication of noise. The power spectrum must be multiplied by sensor characteristics before a value for the variance can be obtained.

By using a sensor whose response is a window function as shown in Figure 22, any slowly varying component of the noise fluctuations will be averaged to zero. The only fluctuations that will be sensed by the detector are those that have periods short compared to the width of the window. The effect of this type of sensor is therefore to reduce the low frequencies that are part of the power spectrum. Because the detector samples over a finite size, only an average signal over the width of the window function is measured. This causes smoothing out the rapidly varying frequencies in the noise signal. This effect results in a rolloff in the higher frequencies of the power spectrum.

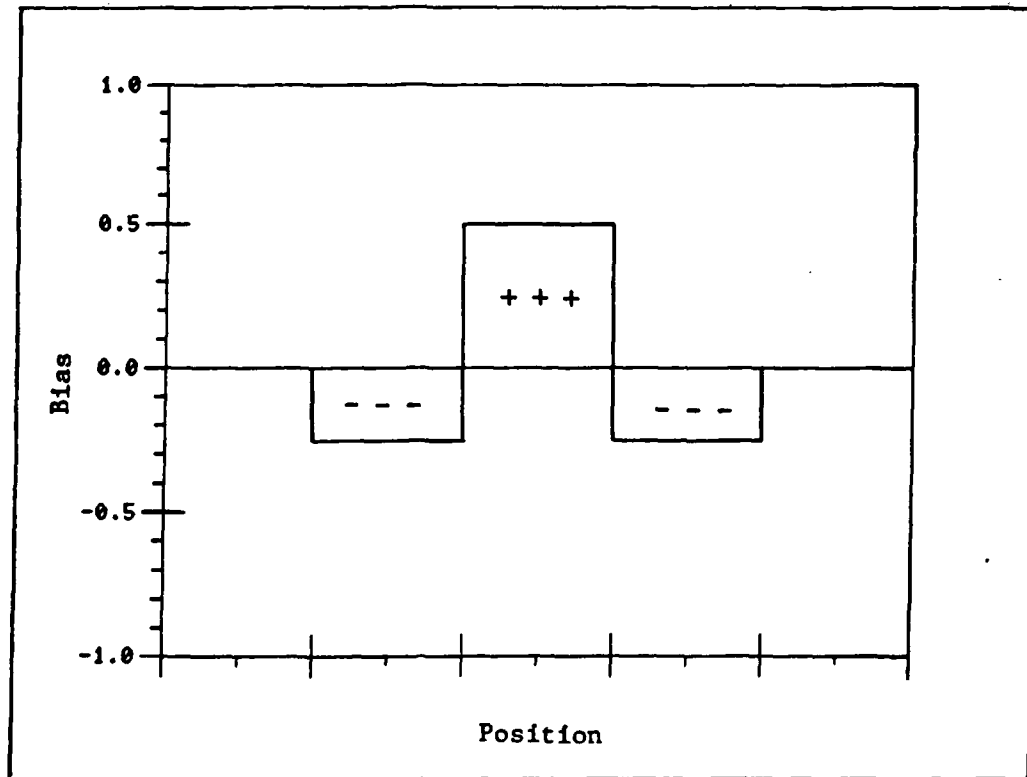


Figure 22. Typical Window Function

The power spectrum can now be integrated to give a variance. This is done numerically by Sanderson (Ref 11), and the actual value depends on the specific window function parameters and the value of  $B$  obtained for the power spectrum. One of the detector types described by Sanderson was chosen that resulted in a variance of  $(1.62)B$ . A value of  $B$  equal to 1.0 was also chosen. The detector type represents one that results in the least amount of background noise variance, and the constant  $B$  represents the background that presents the most variance in background noise.

Because the data obtained by ERIM was given in temper-

ature units, the variance also resulted in temperature units. The conversion to radiance units can be calculated by using the differential form of Planck's law. The result is:

$$\sigma_L^2 = (hc\nu L)/(kT^2) \sigma_T^2 \quad (32)$$

where

$h$  = Planck's constant

$c$  = speed of light

$k$  = Boltzmann's constant

$\nu$  = wavenumber of radiation

$T$  = temperature of background

$L$  = background radiance

This result is only valid for

$$(hc\nu)/(kT) \gg 1 \quad (33)$$

In the IR region of the spectrum with background temperatures near 300 K, this assumption is valid.

The conversion from temperature units gives an answer in spectral radiance units. To convert this to intensity units, the spectral radiance variance is multiplied by the field-of-view of the sensor, the square of the distance to the source, and the bandwidth over which the intensity is measured:

$$\sigma_I^2 = [FOV R^2 d\nu]^2 \sigma_L^2 \quad (34)$$

The following input parameters were used to obtain a result:

$T = 300 \text{ K}$  (normal earth temperature)

$\nu = 2200 \text{ cm}^{-1}$  (near center of bands used)

$\text{FOV} = 10^{-6} \text{ sr}$  (typical sensor)

$d\nu = 25 \text{ cm}^{-1}$  (width of bands used)

The final result is therefore:

$$\sigma^2 = 3.75 \times 10^{-3} R^2 (\text{W/sr})^2 \quad (35)$$

This value was used for the variance in all three bands.

## Appendix D

### Transforms of Band Variation to Angular Variation

In Appendix C, a value for the noise variance was obtained for the three bands used in comparing spectral intensities. Because the signal representations are compared using spherical coordinates, the variances given in Appendix C must be converted to variances in terms of  $\theta$  and  $\phi$ . The covariance matrix for noise could then be added to the covariance matrix of the range distributions to get a total covariance matrix for the distributions.

Assuming small variations, the conversion can be obtained by manipulation of the differentials of the coordinate transforms. Using

$$\rho = (x^2 + y^2 + z^2)^{\frac{1}{2}} \quad (14a)$$

$$\theta = \arctan(y/x) \quad (14b)$$

$$\phi = \arccos[z/(x^2 + y^2 + z^2)^{\frac{1}{2}}] \quad (14c)$$

the differential of the angles in terms of  $x$ ,  $y$ , and  $z$  are

$$d\theta = (\partial\theta/\partial x)dx + (\partial\theta/\partial y)dy \quad (36a)$$

$$= [-y/(x^2 + y^2)]dx + [x/(x^2 + y^2)]dy \quad (36b)$$

Similarly,

$$d\phi = (\partial\phi/\partial x)dx + (\partial\phi/\partial y)dy + (\partial\phi/\partial z)dz \quad (37a)$$

$$\begin{aligned} &= xz(x^2 + y^2)^{-\frac{1}{2}}(x^2 + y^2 + z^2)^{-1}dx \\ &\quad + yz(x^2 + y^2)^{-\frac{1}{2}}(x^2 + y^2 + z^2)^{-1}dy \\ &\quad + (x^2 + y^2)(x^2 + y^2)^{-\frac{1}{2}}(x^2 + y^2 + z^2)^{-1}dz \end{aligned} \quad (37b)$$

$$d\phi = [(x^2+y^2)^{-\frac{1}{2}}(x^2+y^2+z^2)^{-1}][(xz)dx+(yz)dy+(x^2+y^2)dz] \quad (37c)$$

These equations can be used to transform the variance obtained in Appendix C into variances in terms of  $\theta$  and  $\phi$ . The magnitude of the source intensity ( $x$ ,  $y$ , and  $z$ ) must be known though.

The coordinate transform equations allow calculation of all the quantities given any three. At any range, the mean values of  $\theta$  and  $\phi$  are given in the table in Appendix B. Therefore to completely specify all values of  $x$ ,  $y$ , and  $z$ , only one of the variables must be given. For the calculations in Chapter IV, the intensity in band 1 was specified.



## BIBLIOGRAPHY

1. Kneizys, F. X., et al. Atmospheric Transmittance/Radiance: Computer Code LOWTRAN 5. AFGL-TR-80-0067. Hanscom AFB, Massachusetts: Air Force Geophysics Laboratory, 1980.
2. Klein, Miles V. Optics. New York: John-Wiley & Sons, Inc., 1970.
3. Wolfe, William L. and George J. Zissis, Editors. The Infrared Handbook. Ann Arbor, Michigan: Environmental Research Institute of Michigan, 1978.
4. Ashley, G. W., et al. Background Spectral Radiance and Contrast in the Near-UV, Mid-IR, and LWIR Regions. TM6-125PH-438. Pomona: General Dynamics, 1976.
5. Zachor, Alexander S., James A. Holzer, and Frederick G. Smith. IR Signature Study. AFAL-TR-79-1012. Lexington, MA: Honeywell Electro-Optics Center, 1979.
6. Zachor, Alexander S. "Spectral Pattern Recognition in IR Remote Sensing," Applied Optics, 22, (17): 2699-2703 (Sep 1983).
7. Crane, R. B., W. A. Malila, and W. Richardson. "Suitability of the Normal Density Assumption for Processing Multispectral Scanner Data," IEEE Transactions on Geoscience Electronics, GE-10 (4): 158-162 (Oct 1972).
8. Fukunaga, Keinosuke. Introduction to Statistical Pattern Recognition. New York: Academic Press, 1972.
9. Jennings, Alan. Matrix Computation for Engineers and Scientists. Chichester: John Wiley and Sons, Ltd., 1977.
10. Devijver, Pierre A. and Josef Kittler. Pattern Recognition: A Statistical Approach. London: Prentice Hall, 1982.
11. Sanderson, Richard. Infrared Background Characterization (tentative title). Unpublished report. AFWAL/AAWP, Wright-Patterson AFB, OH, 1983.
12. Selby, Samuel M., Editor. Standard Math Tables. Cleveland: CRC Press, Inc., 1974.

13. Lindquist, George H., et al. Threat-Warning Receiver Analysis Code (TRAC). AFWAL-TR-80-1082. Ann Arbor, Mich: Nichols Research Corporation, 1980.
14. LaRocca, Anthony J. and David J. White. Handbook of the Statistics of Various Terrain and Water (Ice) Backgrounds from Selected U.S. Locations. Ann Arbor, Mich: Environmental Institute of Michigan, 1980.
15. International Mathematical and Statistical Libraries. IMSL Library Reference Manual, Ed. 9, Vol. 4. Houston: IMSL, Inc., 1982.
16. McClatchey, R.A., et al. AFCRL Atmospheric Absorption Line Parameters Compilation. AFCRL-TR-73-0096. Bedford, Mass: Air Force Cambridge Research Laboratories, 1973.
17. Herget, William F. and James D. Brasher. "Remote Measurement of Gaseous Pollutant Concentrations Using a Mobile Fourier Transform Interferometer System," Applied Optics, Vol. 18, No. 20: 3404-3420 (Oct 1979).

UNCLASSIFIED

SECURITY CLASSIFICATION OF THIS PAGE

## REPORT DOCUMENTATION PAGE

1a. REPORT SECURITY CLASSIFICATION <b>UNCLASSIFIED</b>		1b. RESTRICTIVE MARKINGS	
2a. SECURITY CLASSIFICATION AUTHORITY		3. DISTRIBUTION/AVAILABILITY OF REPORT Approved for public release; distribution unlimited.	
2b. DECLASSIFICATION/DOWNGRADING SCHEDULE		5. MONITORING ORGANIZATION REPORT NUMBER(S)	
4. PERFORMING ORGANIZATION REPORT NUMBER(S) <b>AFIT/GEP/PH/83D-5</b>		7a. NAME OF MONITORING ORGANIZATION	
6a. NAME OF PERFORMING ORGANIZATION <b>School of Engineering</b>	6b. OFFICE SYMBOL (If applicable) <b>AFIT/EN</b>	7b. ADDRESS (City, State and ZIP Code)	
6c. ADDRESS (City, State and ZIP Code) <b>Air Force Institute of Technology Wright-Patterson AFB, OH 45433</b>		9. PROCUREMENT INSTRUMENT IDENTIFICATION NUMBER	
8a. NAME OF FUNDING/SPONSORING ORGANIZATION <b>AFWAL/AAWP-1</b>	8b. OFFICE SYMBOL (If applicable)	10. SOURCE OF FUNDING NOS.	
8c. ADDRESS (City, State and ZIP Code) <b>Wright-Patterson AFB, OH 45433</b>		PROGRAM ELEMENT NO.	PROJECT NO.
11. TITLE (Include Security Classification) <b>PASSIVE INFRARED RANGING</b>		TASK NO.	WORK UNIT NO.
12. PERSONAL AUTHOR(S) <b>Norman K. Leonpacher, B.S., Capt, USAF</b>			
13a. TYPE OF REPORT <b>MS Thesis</b>	13b. TIME COVERED FROM _____ TO _____	14. DATE OF REPORT (Yr., Mo., Day) <b>1983 December</b>	15. PAGE COUNT <b>91</b>
16. SUPPLEMENTARY NOTATION <div style="text-align: right;">Approved for public release: IAW AFR 190-17. <i>Lynn E. Wolaver</i> 7 Feb 84 LYNN E. WOLAVER Dean for Research and Professional Development Air Force Institute of Technology (AFIT) Wright-Patterson AFB OH 45433</div>			
17. COSATI CODES		18. SUBJECT TERMS (Continue on reverse if necessary and identify by block number)	
FIELD	GROUP	SUB. GR.	
17	05	Infrared Signatures, Infrared Tracking, Atmospheric Windows, Range Finding	
19. ABSTRACT (Continue on reverse if necessary and identify by block number)  Thesis Advisor: Richard B. Sanderson, PhD. Thesis Chairman: David Graham, Major, USAF			
20. DISTRIBUTION/AVAILABILITY OF ABSTRACT <b>UNCLASSIFIED/UNLIMITED <input checked="" type="checkbox"/> SAME AS RPT. <input type="checkbox"/> DTIC USERS <input type="checkbox"/></b>		21. ABSTRACT SECURITY CLASSIFICATION <b>UNCLASSIFIED</b>	
22a. NAME OF RESPONSIBLE INDIVIDUAL <b>David Graham, Major, USAF</b>	22b. TELEPHONE NUMBER (Include Area Code) <b>513-255-5187</b>	22c. OFFICE SYMBOL <b>AFIT/ENP</b>	

The range of an infrared source was estimated by analyzing the atmospheric absorption by  $\text{CO}_2$  in several wavelength intervals of its spectrum. These bandpasses were located at the edge of the  $\text{CO}_2$  absorption band near  $2300 \text{ cm}^{-1}$  ( $4.3 \mu\text{m}$ ).

A specific algorithm to predict range was determined based on numerous computer generated spectra. When tested with these spectra, range estimates within 0.8 km were obtained for ranges between 0 and 18 km.

Accuracy decreased when actual source spectra were tested. Although actual spectra were available only for ranges to 5 km, 63% of these spectra resulted in range estimates that were within 1.6 km of the actual range. Specific spectral conditions that affected the range predictions were found. Methods to correct the deficiencies were discussed.

Errors from atmospheric variations, and the effects of background noise, were also investigated. Limits on accuracy and range resolution were determined.